RESEARCH ARTICLE

Phytochemical profiling and anticancer activity of the n-butanol fraction from Ardisia villosa extract: Inhibition of gastric cancer cell proliferation via cell cycle arrest and senescence induction

Nguyet Mai Hua[1], Van Khang Pham[2], Thi Thanh Huong Le[1], Son Hiep Pham[2], Viet Hoang[3], Thu Huong Trinh[3], Dinh Quang Hung Can[3], Van Hung Hoang[4], Phu Hung Nguyen[3,4]*

1 Faculty of Natural Science and technology, TNU- University of Sciences, Thai Nguyen Province, Vietnam, **2** Faculty of Chemistry, TNU - University of Education, Thai Nguyen Province, Vietnam, **3** Institute for Excellence in Education and Research, Thai Nguyen University (TNU), Thai Nguyen Province, Vietnam, **4** Thai Nguyen University, Thai Nguyen province, Vietnam

* phuhungnguyen@tnu.edu.vn

Abstract

Medicinal plants serve as valuable sources for anticancer drug discovery. This study investigated the anticancer potential of the *n*-butanol fraction from Ardisia villosa extract against breast and gastric cancer cell lines. Phytochemical profiling using UPLC-QToF-MS in both positive and negative ESI modes identified 118 putative compounds, including flavonoids, lignans, alkaloids, triterpenoids, steroids, coumarins, and phenolic acids. The *n*-butanol fraction exhibited dose-dependent antiproliferative effects, with IC_{50} values of 60.2 μg/mL (MCF-7), 85.2 μg/mL (MKN45), and 51.7 μg/mL (AGS). In AGS gastric cancer cells, the extract significantly inhibited 3D tumorsphere formation and suppressed cell migration at concentrations as low as 50 μg/mL ($p < 0.001$). Additionally, *n*-butanol fraction extract markedly induced cellular senescence ($p < 0.01$). Mechanistic investigations revealed that the extract induced G_0/G1 phase arrest by downregulating critical cell cycle regulators, including CCND1, CCNE1, CDK2, CDK3, CDK6, CDK8, and CDK9, while upregulating tumor suppressor and senescence-related genes such as p21, p53, p16, and p27 ($p < 0.01$). Molecular docking analyses further supported these findings by demonstrating strong binding affinities of phytochemicals to key cell cycle regulatory proteins, suggesting a direct molecular basis for their antiproliferative effects. In conclusion, the *n*-butanol fraction of *Ardisia villosa* displays potent anticancer activity, particularly in gastric cancer cells, through multi-targeted mechanisms involving cell cycle inhibition and senescence induction, and holds promise as a natural source for future anticancer therapeutics.

OPEN ACCESS

Citation: Hua NM, Pham VK, Le TTH, Pham SH, Hoang V, Trinh TH, et al. (2026) Phytochemical profiling and anticancer activity of the n-butanol fraction from Ardisia villosa extract: Inhibition of gastric cancer cell proliferation via cell cycle arrest and senescence induction. PLoS One 21(1): e0340458. https://doi.org/10.1371/journal.pone.0340458

Editor: Vinh Le Ba, University of Bergen: Universitetet i Bergen, NORWAY

Received: August 25, 2025

Accepted: December 21, 2025

Published: January 8, 2026

Copyright: © 2026 Hua et al. This is an open access article distributed under the terms of the Creative Commons Attribution License, which permits unrestricted use, distribution, and reproduction in any medium, provided the original author and source are credited.

Data availability statement: All relevant data are within the manuscript and its Supporting Information files.

Funding: This study was financially supported by the research project CS2024-TN06-014

funded by Thai Nguyen University of Sciences, and the research project DH2024-NV-02 funded by Thai Nguyen University. Funder did not play any role in the study design, data collection and analysis, or preparation of the manuscript. There was no additional external funding received for this study.

Competing interests: The authors have declared that no competing interests exist.

Introduction

Globally, gastric cancer remains one of the most prevalent malignancies and has consistently ranked as the fourth leading cause of cancer-related mortality over the past several years [1]. The incidence and mortality rates associated with gastric cancer are steadily increasing, with a notable trend toward younger patient populations [2,3]. Prominent risk factors include a family history of gastric cancer, dietary habits, tobacco smoking, and infections with *Helicobacter pylori* and Epstein–Barr virus (EBV [4].

Surgical resection, chemotherapy, and radiotherapy continue to be the most commonly employed treatment modalities in most countries. Among these methods, surgical intervention seeks to completely remove the tumor; however, it involves inherent risks, such as the possibility of tumor cells entering the bloodstream, which could eventually result in metastasis [5]. Moreover, surgery often involves a prolonged recovery period and is not feasible for patients with advanced metastatic disease. Chemotherapy serves as a primary therapeutic strategy, especially in poorly differentiated gastric cancer, effectively inhibiting tumor progression and reducing tumor mass prior to surgical intervention. Nevertheless, it frequently exerts deleterious effects on patient health due to its severe side effects [6].

The toxic side effects associated with conventional therapies have stimulated research into the development of novel therapeutic agents that offer high efficacy with lower toxicity [7]. In this context, the exploration of natural compounds derived from medicinal plants, with inherent biocompatibility, anticancer potential, and minimal side effects has emerged as a promising research direction [8].

The genus *Ardisia*, comprising approximately 500 species predominantly distributed in tropical and subtropical regions, is widely utilized as ornamental plants, food sources, and traditional medicines [9]. Various studies have demonstrated that species within this genus contain a diverse range of bioactive compounds, including polyphenols, triterpenoid saponins, quinones, and alkylphenols [10]. Several *Ardisia* species have exhibited cytotoxic activities against different cancer cell lines, such as hepatocellular carcinoma, breast cancer, gastric cancer, lung cancer, and colorectal cancer [11,12]. Consequently, *Ardisia* is considered a valuable resource for the development of novel anticancer therapeutics.

Ardisia villosa, a species within the *Ardisia* genus, is found across various regions, including mountainous areas in Northern Vietnam. Phytochemical analyses have revealed the presence of compounds such as triterpenoid saponins, quinones, phenolics, coumarins, cyclic depsipeptides, and flavonoids in *Ardisia* species, which have been associated with anticancer, anti-inflammatory, and antimicrobial properties [13]. Previous studies have also indicated that *Ardisia villosa* possesses inhibitory effects on the proliferation of gastric cancer cells [14]. In traditional medicine, several species of the genus *Ardisia*, including *Ardisia villosa*, have been used as important components in herbal formulations for the treatment of rheumatoid arthritis and for relieving bruises and injuries. In addition, it has also been reported to be used in traditional remedies for the treatment of diseases such as dysentery, pulmonary tuberculosis, haemoptysis, and haematemesis [10].

Although preliminary assessments have suggested the cytotoxic potential of *Ardisia villosa*, the anticancer activity of its extracts and the underlying mechanisms of action remain largely unexplored. Therefore, the objective of the present study is to investigate the anticancer effects of the *n*-butanol fraction of *Ardisia villosa* on AGS human gastric cancer cells.

Materials and methods

Preparation of the *n*-butanol fraction from ardisia villosa leaf extract

Ardisia villosa leaves (voucher TNU2021.07) were gathered in Thai Nguyen Province, Vietnam, and was taxonomically identified by plant taxonomy expert Dr. Thi Thanh Huong Le (Thai Nguyen University) based on the morphological method. Then, the fresh leaves were accurately weighed to 2.5 kg before washing and air-drying. Subsequently, the dried sample was sequentially extracted with 95% ethanol, dichloromethane, deionized water and *n*-butanol, with each extraction cycle performed in triplicate under identical conditions for each solvent. Notably, ethanol extraction was conducted at 70 °C for three hours each cycle. Finally, filtrates were combined and concentrated under reduced pressure in a rotary evaporator to ensure complete removal of all solvents (Fig 1).

Phytochemical profiling of *n*-butanol fraction

The metabolite profiling of the butanol extract and its subfractions of *Ardisia villosa* was performed using an ACQUITY UPLC I-Class Plus system coupled with a Xevo G3 ESI/QTOF high-resolution mass spectrometer (Waters Corporation, USA) [15]. Samples were prepared by dissolving 5 mg of dried extract in 0.5 mL of methanol, filtered through a 0.22 μm membrane, and 1 μL was injected for chromatographic separation using a BEH C18 column. Mass detection was conducted in both positive and negative electrospray ionization modes under optimized conditions. Data acquisition was carried out in full scan mode (m/z 50–1100), and fragmentation information was obtained using low- and high-energy modes. Spectral data were processed using UNIFI software, and peak annotation was performed based on fragmentation patterns compared against the Waters Traditional Medicine Library (Waters Corporation, USA).

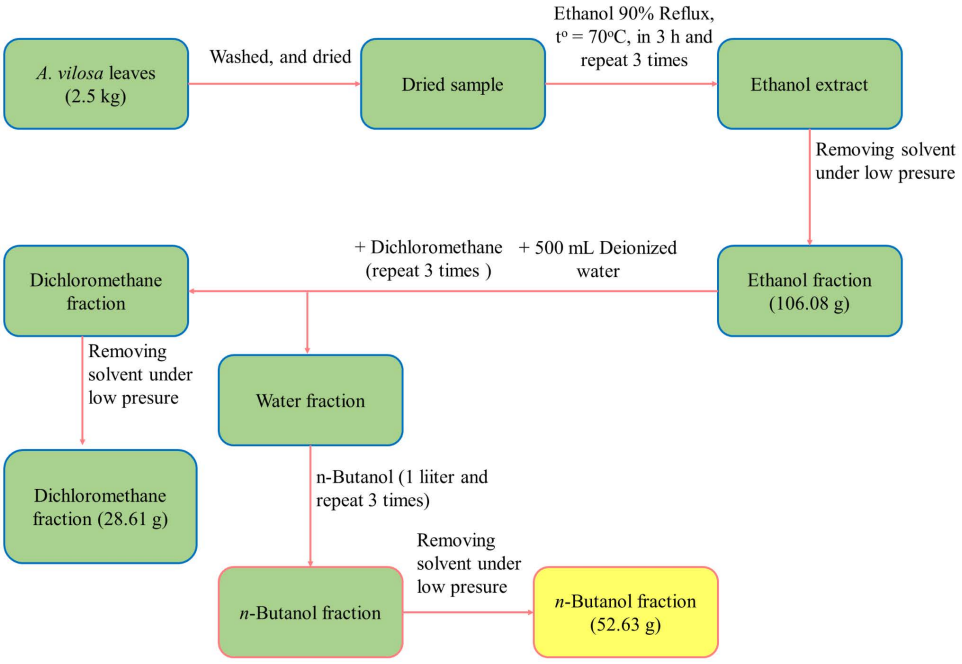

Fig 1. Fractionation scheme of the butanol extract from *Ardisia gigantifolia* leaves.

https://doi.org/10.1371/journal.pone.0340458.g001

Cell culture and MTT assay

MCF7 (breast cancer cells), along with MKN45 and AGS (gastric cancer cells), were seeded into 96-well plates at a density of 1×10^4 cells per well in 100 µL of RPMI 1640 medium, which was enhanced with 10% FBS and 1% ampicillin/streptomycin. The cells were then incubated at 37 °C in a humidified environment containing 5% CO2. After allowing 16–24 hours for cell adhesion, cells were treated with varying concentrations of the butanol extract or its subfractions, specifically 0, 10, 50, 100, 200, or 500 µg/mL. After 48 hours of exposure, morphological alterations were observed and recorded using phase contrast microscopy with a Nikon Ts2 inverted microscope.

The MTT assay was conducted following the reviously protocol [16]. After discarding the spent medium, each well received 100 µL of fresh medium containing MTT at 0.5 mg/mL (Thermo Fisher Scientific, US), and were incubated at 37 °C in 5% CO_2 for 4 h. Thereafter, the MTT solution was removed and replaced with 100 µL of dimethyl sulfoxide (VWR, France), followed by a 15 minutes incubation at 37 °C to solubilize the formazan crystals. Cell viability was assessed by measuring absorbance at 570 nm on a Multiskan Sky spectrophotometer (Thermo Fisher Scientific, USA). Proliferation was expressed as a percentage using the formula provided above.

$$\%\ \text{Cell proliferation} = \frac{\text{OD of the treated sample}}{\text{OD of the control}} \times 100$$

All assays were conducted in triplicate across three independent experiments. IC_{50} values for cell proliferation were determined by nonlinear regression using GraphPad Prism 10.5 in accordance with the manufacturer's guidelines.

Cell migration analysis

Cells were plated in 96-well plates (100 µL/well; 2.0×10^5 cells/well) and allowed to form a uniform monolayer. A linear scratch was made using a 10-µL pipette tip to generate a cell-free gap. Debris and detached cells were removed by washing twice with PBS. The cultures were then exposed to n-buthanol fraction extract (50 and 100) for 24 h. Gap closure, used as an index of migratory capacity, was imaged with a Nikon Ts2 inverted microscope (Tokyo, Japan) and quantified in ImageJ by measuring the gap width at each time point [17]. The remaining open area was expressed as:

$$\text{Open area}\ (\%) = \frac{\text{Width at 24 h}}{\text{Width at 0 h}} \times 100$$

Tumorsphere formation assay

To generate non-adherent culture conditions, 24- or 96-well plates were coated with poly(2-hydroxyethyl methacrylate) (poly-HEMA; 10 mg/mL in 96% ethanol). Briefly, 50 µL (96-well) or 100 µL (24-well) polyHEMA solution was dispensed per well, dried by complete ethanol evaporation at 50–60°C, and the coating step was repeated twice. Wells were then rinsed three times with PBS. During washing and medium changes, pipetting was performed gently to avoid disrupting the polyHEMA layer.

Cells (1,000 cells/well) were seeded in DMEM/F-12 supplemented with 1% penicillin/streptomycin, 0.1% amphotericin B (500 µg/mL), 20 ng/mL EGF, and 0.4% glucose, and treated with ACE at indicated concentrations. After 48 h, tumorspheres were imaged using a Nikon Eclipse Ti2 inverted microscope. Sphere number (clusters ≥ 10 cells) was counted at 100 ×–200 ×, and sphere diameter was measured from 200 × images using ImageJ [17]. Data were expressed as percentages relative to the vehicle control.

Cell cycle analysis

Cell cycle distribution was assessed utilizing a BD Accuri™ C6 Plus flow cytometer (BD Biosciences, USA) as previously described [18]. A total of $2 \times 10^{\wedge 4}$ cells were seeded in 24-well plates and incubated in RPMI 1640 medium for 24 hours.

Subsequently, the cells were treated with fresh medium containing subfraction of butanol extract at varying concentrations ranging from 0 to 200 µg/mL for a duration of 48 hours. Post-treatment, the cells were fixed in 70% ethanol and stained with propidium iodide (PI) for 30 minutes. Following staining, cells were collected through trypsinization and centrifuged at 13,000 rpm for 5 minutes. Flow cytometric analysis was conducted to evaluate DNA content and cell cycle phases, with all experiments performed in triplicate to ensure reproducibility [18].

Cell senescence assay

Senescence was evaluated through histochemical staining using Senescence Cells Histochemical Staining Kit (Sigma-Aldrich, France), according to the manufacturer's protocol. The cells were initially washed twice with 1 × phosphate buffered saline (PBS) solution to remove any residual medium or debris. Subsequently, cells were fixed with 1 × Fixation buffer and incubated the plate for 10–15 minutes at room temperature to preserve their structural integrity. After fixation, the Fixation buffer was discarded, and the cells were rinsed twice more with 1 × PBS, using 500 µL per wash to ensure complete removal of the fixative. Subsequently, 50 µL Staining mix solution containing senescence-associated β-galactosidase (SA-β-gal) was applied to each well. The cells were then cultured at 37°C in the absence of light for 2 hours to facilitate the detection of SA-β-gal activity, which serves as a marker for cellular senescence. Following the incubation period, the cells were examined under a light inverted microscope at 100 × magnification. The presence of senescent cells was confirmed by the characteristic blue staining, which was visualized and documented through microscopic imaging [19]. The experiments were repeated 3 times for each condition

Real-time PCR analysis for mRNA expression

Cancer cells were cultured in 6-well plates at a density of 2×10^5 cells per well and subjected to a subfraction of butanol extract at its IC_{50} concentration for a duration of 24 h. Subsequent to the treatment, total RNA was extracted utilizing TRIzol reagent (Invitrogen Thermo Fisher Scientific, US) in accordance with established protocols. Following chloroform-induced phase separation and ethanol-mediated RNA precipitation, the RNA was washed with 70% ethanol, air-dried, and reconstituted in nuclease-free water. The yield and purity of RNA were quantified using a NanoDrop spectrophotometer. Quantitative real-time PCR were conducted utilizing the BIOFACT 2 × One-Step SYBR Green RT-qPCR kit (BIOFACT, Korea) on a qTower³ thermal cycler (Analytik Jena, Germany), with each reaction comprising 20 ng of total RNA. The thermal profile included an initial denaturation at 95 °C for 15 minutes, followed by 95 °C for 20 seconds and 60 °C for 20 seconds for 40 cell cycles. Primer sequences used are listed in S1 Table. HPRT1 was used as the reference gene, and relative expression was calculated using the $2^{-\Delta\Delta Ct}$ method [20]. All experiments were conducted in three independent replicates.

Molecular docking

Ligand and protein preparation. The chemical structures of the investigated compounds were either retrieved from the PubChem database (https://pubchem.ncbi.nlm.nih.gov) in SDF format or manually drawn using ChemDraw 23.1.1. Ligands were prepared using the LigPrep module in Schrödinger Maestro (Release 2024−3), which generated all plausible tautomeric and stereoisomeric forms, assigned ionization states at pH 7.0 ± 2.0, and optimized each structure to its lowest-energy 3D conformation using the OPLS4 force field.

The crystal structures of cyclin-dependent kinases CDK2, CDK3, CDK4, CDK6, CDK8, and CDK9 were retrieved from the Protein Data Bank (PDB IDs: 2R3I, 8H4R, 7SJ3, 5L2S, 5HBJ, and 8I0L, respectively). Protein structures were processed using the Protein Preparation Wizard. During preparation, bond orders were reassigned, missing hydrogens were added, and crystallographic water molecules not involved in ligand interactions were removed. The protonation states of ionizable residues were predicted using PROPKA at pH 7.4, and hydrogen-bonding networks were optimized accordingly. For co-crystallized ligands and hetero groups, Epik was used to determine protonation and tautomeric states at pH 7.4 ± 2.0.

Molecular docking and validation. For each CDK target, the binding site was defined based on the location of the co-crystallized ligand in the corresponding PDB structure. The receptor grid boxes used for docking were centered on this ligand and adjusted to encompass the entire binding pocket. Grid coordinates and dimensions for each protein target are listed in Table 1.

To validate the docking protocol, the co-crystallized ligands were re-docked into their original binding sites using the Glide XP (extra precision). The resulting poses were compared with the crystal structures by calculating the root-mean-square deviation (RMSD), and docking was considered reliable when RMSD values were below 2.0 Å. Subsequently, 118 prepared ligands were docked against all six CDK targets using Glide XP.

MM-GBSA binding free energy estimation. The binding free energies of the top-ranked docking poses were evaluated using the Prime MM-GBSA method (Molecular Mechanics with Generalized Born Surface Area), which is widely recognized as a robust method for estimating relative binding affinities of ligand–protein complexes [21]. Calculations were performed using the VSGB solvation model and the OPLS4 force field. Binding free energy (ΔG_{bind}) was calculated as:

$$\Delta G_{bind} = G_{complex} - G_{protein} - G_{ligand}$$

where $G_{complex}$ represents the free energy of the complex, and $G_{protein}$ and G_{ligand} represent the MM-GBSA energies of the unbound protein and ligand, respectively.

Data analysis

The data gathered were examined using the specialized software GraphPad Prism 10.5 (GraphPad Software, San Diego, CA, USA). Mann-Whitney and one-way ANOVA test were employed for statistical analysis, with a p-value of less than 0.05 considered as statistically significant.

Results

Phytochemical profiling of the *n*-butanol fraction

Compound identification was performed using exact mass measurements, fragmentation patterns obtained under both high- and low-energy collision conditions, and spectral matching with library data. The respective total ion chromatograms (TICs) are shown in Fig 2 which illustrates the chromatograms produced under two ionization conditions: (A) negative and (B) positive. Positive electrospray ionization (ESI) mode exhibited superior ionization efficiency, as indicated by a greater number of detected ion signals compared to the negative ion mode. During data preprocessing, only peaks with signal

Table 1. Receptor grid box parameters for CDK proteins.

Grid box parameters	CDK2	CDK3	CDK4	CDK6	CDK8	CDK9
Center_x	1.932	24.472	11.657	21.986	−4.633	53.649
Center_y	27.635	−98.257	−39.053	38.630	12.823	−17.358
Center_z	7.948	12.691	10.364	−9.236	−11.182	−12.352
Innerbox_x	10	10	10	10	10	10
Innerbox_y	10	10	10	10	10	10
Innerbox_z	10	10	10	10	10	10
Outerbox_x	23.434	23.969	26.622	26.521	23.957	24.671
Outerbox_y	23.434	23.969	26.622	26.521	23.957	24.671
Outerbox_z	23.434	23.969	26.622	26.521	23.957	24.671

https://doi.org/10.1371/journal.pone.0340458.t001

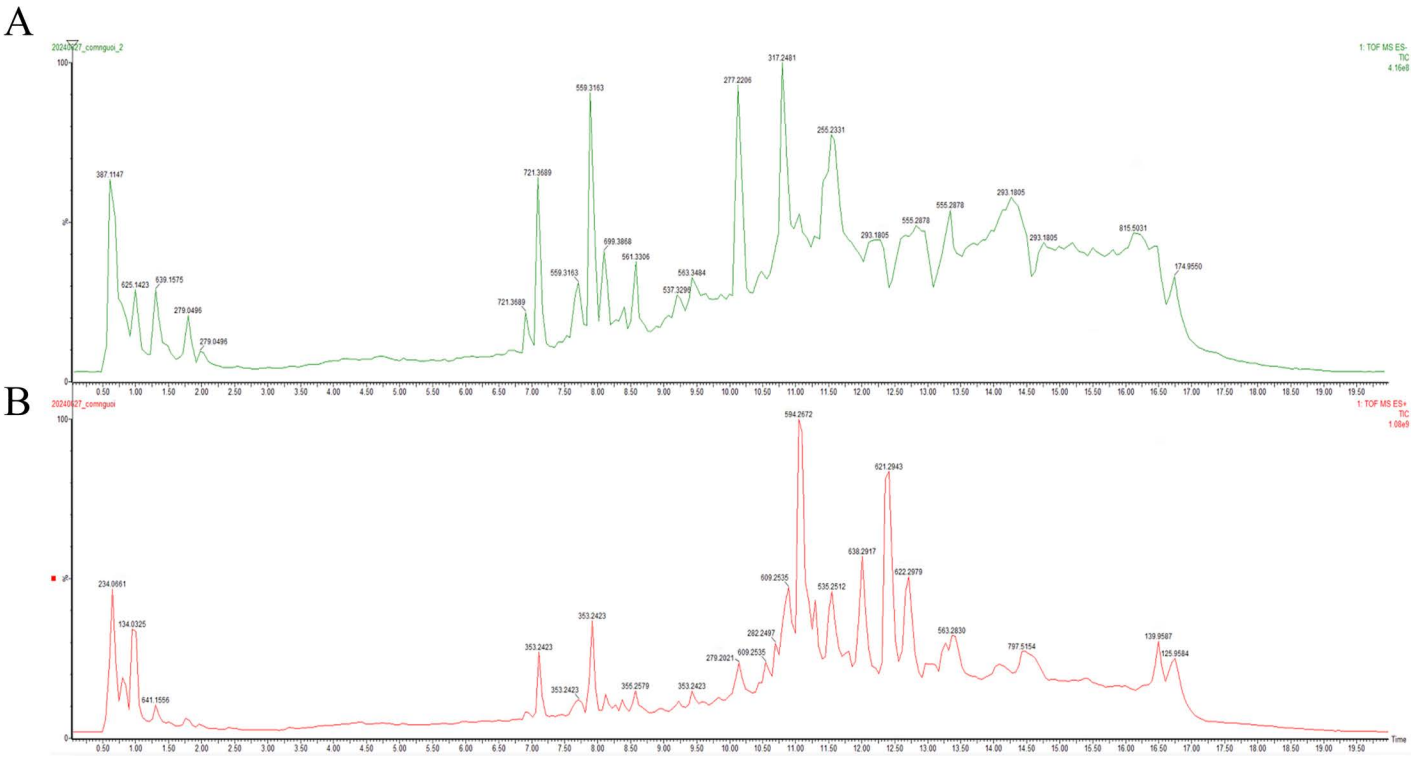

Fig 2. UPLC-QToF-MS chromatographic profiles of *n*-butanol soluble fractions isolated from *Ardisia villosa*. Extract under (A) negative and (B) positive ESI modes.

https://doi.org/10.1371/journal.pone.0340458.g002

intensities above 5000 counts were annotated, and a mass error tolerance of 5 ppm was applied to match experimental data with theoretical values.

The compounds were arranged according to observed RT. A total of one hundred and eighteen compounds were tentatively identified including ten flavonoid compounds, ten lignans, twenty-two alkaloids, thirty-seven triterpenoids, thirteen steroids, 5 coumarin compounds, twelve phenolic & aromatic compounds and other funtional ingredients. It is possible to check the distribution of the determined secondary metabolites in the analyzed sample. The 118 detected compounds with UPLC-QToF-MS in both negative and positive mode are listed in Table 2, along with names of the compounds; formula; expected mass (Da); observed mass (Da); observed (m/z); mass error (mDa); observed RT (min); class; pathway.

Anti-proliferation activity of *n*-butanol fraction. The antiproliferative activity of the ethanol fraction (crude extract), n-butanol, and Dichlorometane fraction fraction was evaluated against three cancer cell lines, including breast cancer (MCF-7) and gastric cancer (MKN45 and AGS), using the MTT assay. The half-maximal inhibitory concentration (IC_{50}) values of the extracts and fractions shown in Table 3 (and see more in S2 Table, S3 Table, and S4 Table) indicate that the effects on cell proliferation differed among the crude extract (ethanol extract) and fractions, as well as among the tested cell lines. The *n*-butanol fraction exhibited the strongest activity, showing low IC_{50} values with narrow confidence intervals in the evaluated cell lines, particularly in AGS cells (51.7 μg/mL). In contrast, the ethanol fraction showed the weakest activity, as reflected by higher IC_{50} values, most notably in AGS cells (167.4 μg/mL). Among the cell lines, AGS appeared more sensitive than MCF7 and MKN45 to the tested fractions. Therefore, the *n*-butanol fraction effect in AGS cells was selected for subsequent mechanistic investigations and more analyses.

As shown in Fig 3, the cell viability of all tested cell lines decreased in a dose-dependent manner across concentrations ranging from 0 μg/mL to 500 μg/mL. Even at the initial concentration of 10 μg/mL, a reduction in proliferation was observed, with MCF-7 and AGS cell viability decreasing to 74.6 ± 3.9% and 69.0 ± 2.7%, respectively. Notably,

Table 2. Phytochemical compound of *n*-butanol fraction from *Ardisia villosa*.

No.	Compound	Formula	Expected mass (Da)	Observed mass (Da)	Observed (m/z)	Mass Error (mDa)	Observed RT (min)	Class	Pathway
1	**Oleracein D**	$C_{31}H_{37}NO_{17}$	695.206	695.205	696.213	−0.782	0.665	Betalain alkaloids	Alkaloids
2	**Apiosylskimmin**	$C_{20}H_{24}O_{12}$	456.127	456.126	457.134	−0.498	0.665	Simple coumarins	Shikimates and Phenyl-propanoids
3	**Ononin**	$C_{22}H_{22}O_{9}$	430.126	430.126	431.133	−0.655	0.665	Isoflavones	Shikimates and Phenyl-propanoids
4	**Decursitin F**	$C_{16}H_{16}O_{6}$	304.095	304.096	305.103	1.412	0.666	Pyrano-coumarins	Shikimates and Phenyl-propanoids
5	**Nordracorubin**	$C_{31}H_{22}O_{5}$	474.147	474.146	475.154	−0.362	0.671	Flavans	Shikimates and Phenyl-propanoids
6	**Bruceene**	$C_{20}H_{26}O_{8}$	394.163	394.162	395.170	−0.417	0.674	Quassinoids	Terpenoids
7	**Podophyllotoxin**	$C_{22}H_{22}O_{8}$	414.131	414.133	415.140	1.534	0.675	Aryl-naphthalene	Shikimates and Phenyl-propanoids
8	**1,7-Bis (4-hydroxyphenyl)-hepta-4E,6E-dien-3-one**	$C_{19}H_{18}O_{3}$	294.126	294.127	295.134	1.211	0.729	Linear diaryl-heptanoids	Shikimates and Phenyl-propanoids
9	**n-(1,7-dimethoxy-phenanthren-2-yl)-acetamide**	$C_{18}H_{17}NO_{3}$	295.121	295.122	296.129	0.914	0.730	Phenanth-renes	Shikimates and Phenyl-propanoids
10	**Xantholide A**	$C_{15}H_{18}O_{2}$	230.131	230.130	231.138	−0.379	0.846	Guaiane sesqui-terpenoids	Terpenoids
11	**Kushenol W**	$C_{21}H_{22}O_{7}$	386.137	386.137	387.145	0.706	0.868	Flavanones	Shikimates and Phenyl-propanoids
12	**Leonticine**	$C_{20}H_{25}NO_{3}$	327.183	327.182	328.190	−1.011	0.868	Monomeric stilbenes	Shikimates and Phenyl-propanoids
13	**Didemethoxyl-curcumin**	$C_{19}H_{16}O_{4}$	308.105	308.105	309.113	0.541	0.981	Linear diaryl-heptanoids	Shikimates and Phenyl-propanoids
14	**Isohypericin**	$C_{30}H_{16}O_{8}$	504.085	504.084	505.092	−0.191	0.985	Anthra-quinones and anthrones	Polyketides
15	**Arnebinol**	$C_{16}H_{20}O_{2}$	244.146	244.146	245.154	0.050	1.012	Meromono-terpenoids	Terpenoids
16	**Lusianthridin**	$C_{15}H_{14}O_{3}$	242.094	242.095	243.102	0.340	1.252	Phenanth-renes	Shikimates and Phenyl-propanoids
17	**Epigallocatechin (4beta,8)-gallocatechin**	$C_{30}H_{26}O_{14}$	610.132	610.135	611.142	2.787	1.310	Pro-anthocyanins	Shikimates and Phenyl-propanoids
18	**7-O-Methylmorroniside**	$C_{18}H_{28}O_{11}$	420.163	420.161	421.169	−1.694	1.350	Iridoids monoterpenoids	Terpenoids
19	**Flazin**	$C_{17}H_{12}N_{2}O_{4}$	308.080	308.078	309.086	−1.211	1.490	Carboline alkaloids	Alkaloids
20	**3-O-Methylellagic acid**	$C_{15}H_{8}O_{8}$	316.022	316.022	317.030	0.394	1.763	Gallotannins	Shikimates and Phenyl-propanoids
21	**8-Hydroxydihydro-chelerythrine**	$C_{21}H_{19}NO_{5}$	365.126	365.128	366.135	1.299	5.614	Isoquinoline alkaloids	Alkaloids
22	**Eupalinolide A**	$C_{24}H_{30}O_{9}$	462.189	462.190	463.198	1.322	7.124	Germacrane sesqui-terpenoids	Terpenoids
23	**Erysimoside**	$C_{35}H_{52}O_{14}$	696.336	696.337	697.344	1.390	7.127	Cardenolides	Terpenoids
24	**Taurocholic acid**	$C_{26}H_{45}NO_{7}S$	515.292	515.294	516.301	2.086	7.129	Cholane steroids	Terpenoids
25	**Ganoderenic acid A**	$C_{30}H_{42}O_{7}$	514.293	514.291	515.299	−1.804	7.129	Lanostane, Tirucal-lane and Euphane triterpenoids	Terpenoids

(Continued)

Table 2. (Continued)

No.	Compound	Formula	Expected mass (Da)	Observed mass (Da)	Observed (m/z)	Mass Error (mDa)	Observed RT (min)	Class	Pathway
26	**Lappaol H**	$C_{40}H_{46}O_{14}$	750.289	750.292	751.299	2.987	7.132	Dibenzyl-butyrolactone lignans	Shikimates and Phenyl-propanoids
27	**Capnoidine**	$C_{20}H_{17}NO_6$	367.106	367.105	368.112	−1.017	7.133	Isoquinoline alkaloids	Alkaloids
28	**Kansuinin E**	$C_{41}H_{47}NO_{14}$	777.300	777.296	778.303	−3.891	7.133	Jatrophane diterpenoids	Terpenoids
29	**Ganoderic acid B**	$C_{30}H_{44}O_7$	516.309	516.307	517.314	−2.202	7.666	Lanostane, Tirucallane and Euphane triterpenoids	Terpenoids
30	**Tenuifolin**	$C_{36}H_{56}O_{12}$	680.377	680.379	681.386	1.986	7.685	Oleanane triterpenoids	Terpenoids
31	**N,N′-Dicarbazyl**	$C_{24}H_{16}N_2$	332.131	332.131	333.139	−0.004	7.685	Carboline alkaloids	Alkaloids
32	**Cichorioside B**	$C_{21}H_{28}O_{10}$	440.168	440.170	441.177	1.442	7.774	Guaiane sesqui-terpenoids	Terpenoids
33	**Daturametelin I**	$C_{34}H_{48}O_{10}$	616.325	616.322	617.330	−2.294	7.917	Ergostane steroids	Terpenoids
34	**6alpha-Acetoxy-5-epilimonin**	$C_{28}H_{32}O_{10}$	542.252	542.253	543.260	0.973	7.926	Limonoids	Terpenoids
35	**Pulchinenoside B**	$C_{53}H_{86}O_{22}$	1074.561	1074.563	1075.570	1.826	7.928	Lupane triterpenoids	Terpenoids
36	**Lactucin**	$C_{15}H_{16}O_5$	276.100	276.100	277.108	0.511	7.930	Guaiane sesqui-terpenoids	Terpenoids
37	**Andrographatoside**	$C_{26}H_{42}O_9$	498.283	498.285	499.292	2.279	7.931	Labdane diterpenoids	Terpenoids
38	**Agrimol A**	$C_{37}H_{46}O_{12}$	682.299	682.299	683.306	0.090	8.136	Oligomeric phlorogluci-nols (phloro-tannins)	Polyketides
39	**Nimbolidin C**	$C_{37}H_{50}O_{12}$	686.330	686.331	687.339	1.031	8.138	Limonoids	Terpenoids
40	**Curcumadiol**	$C_{15}H_{26}O_2$	238.193	238.194	239.201	0.912	8.140	Guaiane sesqui-terpenoids	Terpenoids
41	**Evoprenine**	$C_{20}H_{21}NO_4$	339.147	339.146	340.153	−0.924	8.141	Acridone alkaloids	Alkaloids
42	**6-Aldehydo-7-methoxyiso-ophiopogonanone B**	$C_{20}H_{16}O_7$	354.110	354.112	355.119	1.242	8.143	Chromones	Polyketides
43	**Galloylpaeoniflorin**	$C_{30}H_{32}O_{15}$	632.174	632.176	633.183	2.065	8.161	Pinane monoterpenoids	Terpenoids
44	**Wuweizi alcohol A**	$C_{24}H_{32}O_7$	432.215	432.214	433.222	−0.402	8.300	Dibenzo-cyclooctadienes lignans	Shikimates and Phenyl-propanoids
45	**Kirenol**	$C_{20}H_{34}O_4$	338.246	338.247	339.255	1.573	8.393	Pimarane and Isopimarane diterpenoids	Terpenoids
46	**Cyclocurcumin**	$C_{21}H_{20}O_6$	368.126	368.127	369.134	1.210	8.394	Linear diarylheptanoids	Shikimates and Phenyl-propanoids
47	**Magnaldehyde B**	$C_{18}H_{16}O_3$	280.110	280.110	281.117	−0.336	8.550	Neolignans	Shikimates and Phenyl-propanoids
48	**Ganoderic acid gamma**	$C_{30}H_{44}O_7$	516.309	516.307	517.314	−1.645	8.592	Lanostane, Tirucallane and Euphane triterpenoids	Terpenoids
49	**Ganoderic acid alpha**	$C_{32}H_{46}O_9$	574.314	574.317	575.324	2.524	8.938	Lanostane, Tirucallane and Euphane triterpenoids	Terpenoids

(Continued)

Table 2. (Continued)

No.	Compound	Formula	Expected mass (Da)	Observed mass (Da)	Observed (m/z)	Mass Error (mDa)	Observed RT (min)	Class	Pathway
50	**Licoflavone A**	$C_{20}H_{18}O_4$	322.121	322.120	323.128	−0.212	8.961	Flavones	Shikimates and Phenyl-propanoids
51	**1-Methyl-2-undecyl-4(1H)-quinolone**	$C_{21}H_{31}NO$	313.241	313.239	314.247	−1.283	9.247	Quinoline alkaloids	Alkaloids
52	**Stigmast-4-ene-3,6-dione**	$C_{29}H_{46}O_2$	426.350	426.348	427.355	−2.134	9.275	Stigmastane steroids	Terpenoids
53	**Belladonnine**	$C_{34}H_{42}N_2O_4$	542.314	542.316	543.324	1.775	9.477	Tropane alkaloids	Alkaloids
54	**1-Methyl-2-[(Z)-7-tridecenyl]-4(1H)-quinolone**	$C_{23}H_{33}NO$	339.256	339.255	340.262	−1.356	9.488	Quinoline alkaloids	Alkaloids
55	**Meranzin hydrate**	$C_{15}H_{18}O_5$	278.115	278.116	279.123	0.542	9.489	Simple coumarins	Shikimates and Phenyl-propanoids
56	**Cissogenin**	$C_{21}H_{34}O_5$	366.241	366.240	367.247	−0.818	9.617	Pregnane steroids	Terpenoids
57	**Phytolaccagenin**	$C_{31}H_{48}O_7$	532.340	532.339	533.346	−1.012	9.638	Oleanane triterpenoids	Terpenoids
58	**Ajugasterone C-2,3,20,22-diacetonide**	$C_{33}H_{52}O_7$	560.371	560.374	561.381	2.279	9.654	Ecdysteroids	Terpenoids
59	**Sophoranodichromane A**	$C_{26}H_{30}O_5$	424.189	424.189	425.196	0.267	9.682	Flavanones	Shikimates and Phenyl-propanoids
60	**Pterodontoside H**	$C_{21}H_{36}O_7$	400.246	400.247	401.254	1.029	9.830	Eudesmane sesqui-terpenoids	Terpenoids
61	**Picrasinoside G**	$C_{28}H_{44}O_{12}$	572.283	572.286	573.293	2.630	9.905	Quassinoids	Terpenoids
62	**Nomilin**	$C_{28}H_{34}O_9$	514.220	514.222	515.230	1.945	10.139	Limonoids	Terpenoids
63	**Cinobufagin**	$C_{26}H_{34}O_6$	442.236	442.238	443.245	2.011	10.154	Bufa-dienolides	Terpenoids
64	**Gentianamine**	$C_{11}H_{11}NO_3$	205.074	205.074	206.081	−0.361	10.219	Pyridine alkaloids	Alkaloids
65	**Neohecogenin-3-O-beta-D-glucopyranoside**	$C_{33}H_{52}O_9$	592.361	592.364	593.371	2.804	10.234	Spirostane steroids	Terpenoids
66	**11-Hydroxy-9-tridecenoic acid**	$C_{13}H_{24}O_3$	228.173	228.174	229.181	1.140	10.473	Hydroxy fatty acids	Fatty acids
67	**Cucurbitacin B**	$C_{32}H_{46}O_8$	558.319	558.317	559.324	−2.494	10.646	Cucurbitane triterpenoids	Terpenoids
68	**Clinopodiside F**	$C_{49}H_{82}O_{20}$	990.540	990.540	991.547	−0.099	10.756	Oleanane triterpenoids	Terpenoids
69	**Daturametelin D**	$C_{29}H_{40}O_5$	436.261	436.262	437.270	0.932	10.834	Ergostane steroids	Terpenoids
70	**Marsdenoside B**	$C_{45}H_{68}O_{14}$	832.461	832.462	833.469	1.019	10.896	Pregnane steroids	Terpenoids
71	**24-Acetate alisol F**	$C_{32}H_{50}O_6$	530.361	530.362	531.369	1.157	10.920	Fusidane triterpenoids	Terpenoids
72	**Agroastragaloside IV**	$C_{49}H_{80}O_{20}$	988.524	988.521	989.528	−3.627	10.964	Cucurbitane triterpenoids	Terpenoids
73	**Syringaresinolmono-beta-D-glucoside**	$C_{24}H_{28}O_{10}$	592.252	592.251	593.258	−0.973	11.109	Furofuranoid lignans	Shikimates and Phenyl-propanoids
74	**Blestrianol B**	$C_{37}H_{32}O_7$	588.215	588.218	589.225	2.909	11.115	Phenanth-renes	Shikimates and Phenyl-propanoids
75	**Brucine**	$C_{23}H_{26}N_2O_4$	394.189	394.188	395.195	−1.426	11.535	Aspidosperma-Iboga hybrid type (Vinca alkaloids)	Alkaloids

(Continued)

Table 2. (Continued)

No.	Compound	Formula	Expected mass (Da)	Observed mass (Da)	Observed (m/z)	Mass Error (mDa)	Observed RT (min)	Class	Pathway
76	**Soyasaponin III**	$C_{42}H_{68}O_{14}$	812.492	812.495	813.502	2.725	11.538	Oleanane triterpenoids	Terpenoids
77	**Huangqiyenin B**	$C_{36}H_{60}O_{10}$	652.419	652.417	653.425	−1.313	11.580	Oleanane triterpenoids	Terpenoids
78	**Lappaol B**	$C_{31}H_{34}O_{9}$	550.220	550.222	551.229	1.576	11.593	Dibenzyl-butyrolactone lignans	Shikimates and Phenyl-propanoids
79	**Curculigo saponin A**	$C_{36}H_{60}O_{9}$	636.424	636.424	637.431	0.346	11.605	Cycloartane triterpenoids	Terpenoids
80	**Interiotherin C**	$C_{30}H_{36}O_{10}$	556.231	556.231	557.238	−0.229	11.614	Dibenzo-cycloocta-dienes lignans	Shikimates and Phenyl-propanoids
81	**Simalikalactone D**	$C_{25}H_{34}O_{9}$	478.220	478.219	479.226	−1.136	11.677	Quassinoids	Terpenoids
82	**Gypenoside XVII**	$C_{48}H_{82}O_{18}$	946.550	946.546	947.553	−4.017	11.912	Dammarane and Protostane triterpenoids	Terpenoids
83	**Icariin**	$C_{33}H_{40}O_{15}$	676.237	676.233	677.241	−3.292	12.025	Flavonols	Shikimates and Phenyl-propanoids
84	**Cistanoside C**	$C_{31}H_{38}O_{15}$	638.221	638.223	639.231	2.404	12.027	Cinnamic acids and derivatives	Shikimates and Phenyl-propanoids
85	**Carmichaeline**	$C_{22}H_{35}NO_{4}$	377.257	377.255	378.262	−1.437	12.160	Terpenoid alkaloids	Alkaloids
86	**Tenacissoside L**	$C_{42}H_{72}O_{16}$	832.482	832.480	833.487	−2.339	12.208	Pregnane steroids	Terpenoids
87	**Hordatine B**	$C_{29}H_{40}N_{8}O_{5}$	580.312	580.311	581.318	−1.252	12.315	Neolignans	Alkaloids
88	**Tsugaric acid B**	$C_{33}H_{52}O_{5}$	528.381	528.382	529.389	0.577	12.364	Lanostane, Tirucallane and Euphane triterpenoids	Terpenoids
89	**Lablaboside C**	$C_{60}H_{96}O_{28}$	1264.609	1264.610	1265.617	1.158	12.403	Oleanane triterpenoids	Terpenoids
90	**Vaccaroside B**	$C_{60}H_{94}O_{29}$	1278.588	1278.582	1279.589	−6.100	12.406	Oleanane triterpenoids	Terpenoids
91	**Pingpeimine A**	$C_{27}H_{45}NO_{5}$	463.330	463.331	464.339	1.542	12.421	Steroidal alkaloids	Alkaloids
92	**Delphatine**	$C_{26}H_{43}NO_{7}$	481.304	481.303	482.310	−1.333	12.441	Terpenoid alkaloids	Alkaloids
93	**Neferine**	$C_{38}H_{44}N_{2}O_{6}$	624.320	624.317	625.324	−2.932	12.737	Isoquinoline alkaloids	Alkaloids
94	**Ephedradine B**	$C_{29}H_{38}N_{4}O_{5}$	522.284	522.286	523.293	1.678	12.784	Polyamines	Alkaloids
95	**Adhyperforin**	$C_{36}H_{54}O_{4}$	550.402	550.401	551.409	−0.932	12.819	Poly-prenylated cyclic polyketides (Hop mero-terpenoids)	Polyketides
96	**Senbusine B**	$C_{23}H_{37}NO_{6}$	423.262	423.261	424.268	−0.990	12.842	Terpenoid alkaloids	Alkaloids
97	**Sipeimine**	$C_{27}H_{43}NO_{3}$	429.324	429.326	430.333	1.365	13.053	Steroidal alkaloids	Alkaloids
98	**Lyciumin A**	$C_{42}H_{51}N_{9}O_{12}$	873.366	873.365	874.372	−0.695	13.063	Cyclic peptides	Amino acids and Peptides
99	**Yemuoside YM14**	$C_{58}H_{92}O_{25}$	1042.535	1042.532	1043.539	−3.317	13.149	Oleanane triterpenoids	Terpenoids
100	**Phytolaccagenic acid**	$C_{31}H_{48}O_{6}$	516.345	516.346	517.354	1.306	13.305	Oleanane triterpenoids	Terpenoids
101	**Ganolactone**	$C_{27}H_{36}O_{6}$	456.251	456.249	457.257	−1.749	13.700	Lanostane, Tirucallane and Euphane triterpenoids	Terpenoids

(Continued)

Table 2. (Continued)

No.	Compound	Formula	Expected mass (Da)	Observed mass (Da)	Observed (m/z)	Mass Error (mDa)	Observed RT (min)	Class	Pathway
102	**Delbrusine**	$C_{27}H_{43}NO_7$	493.304	493.305	494.312	0.813	13.710	Terpenoid alkaloids	Alkaloids
103	**Tigloylgomisin H**	$C_{28}H_{36}O_8$	500.241	500.243	501.250	1.823	14.015	Dibenzo-cyclooctadienes lignans	Shikimates and Phenyl-propanoids
104	**Protostemotinine**	$C_{23}H_{29}NO_6$	415.199	415.199	416.206	−0.360	14.544	Stemona alkaloids	Alkaloids
105	**Sanggenon C**	$C_{40}H_{36}O_{12}$	708.221	708.220	709.228	−0.400	14.911	Chalcones	Shikimates and Phenyl-propanoids
106	**Physanol A**	$C_{36}H_{50}O_4$	546.371	546.371	547.379	0.573	15.226	Ecdysteroids	Terpenoids
107	**Cumambrin A**	$C_{17}H_{22}O_5$	306.147	306.146	307.153	−1.140	15.798	Guaiane sesquiterpenoids	Terpenoids
108	**Physanol B**	$C_{36}H_{52}O_4$	548.387	548.387	549.394	0.310	16.221	Ecdysteroids	Terpenoids
109	**Daturametelin C**	$C_{29}H_{40}O_5$	468.288	468.290	469.297	2.253	16.243	Ergostane steroids	Terpenoids
110	**Aurapten**	$C_{19}H_{22}O_3$	298.157	298.157	299.164	0.074	16.261	Simple coumarins	Shikimates and Phenyl-propanoids
111	**Marsdenoside C**	$C_{47}H_{68}O_{14}$	856.461	856.458	857.465	−3.152	16.275	Pregnane steroids	Terpenoids
112	**Phytolacca cerebroside**	$C_{48}H_{93}NO_{10}$	843.680	843.678	844.685	−2.314	16.359	Neutral glycosphingolipids	Fatty acids
113	**Picroside III**	$C_{25}H_{30}O_{13}$	538.169	538.169	539.176	0.424	16.508	Iridoids monoterpenoids	Terpenoids
114	**Isoaloeresin A**	$C_{28}H_{28}O_{11}$	540.163	540.165	541.172	1.373	16.509	Chromones	Polyketides
115	**1-Vinyl-4-methoxy-beta-carboline**	$C_{14}H_{12}N_2O$	224.095	224.095	225.102	−0.297	16.529	Carboline alkaloids	Alkaloids
116	**Kushenol B**	$C_{30}H_{36}O_6$	492.251	492.253	493.260	1.656	16.556	Flavanones	Shikimates and Phenyl-propanoids
117	**Asterinin A**	$C_{25}H_{33}N_5O_8$	531.233	531.235	532.242	1.720	16.784	Tripeptides	Amino acids and Peptides
118	**Marmesinin**	$C_{20}H_{24}O_9$	408.142	408.144	409.151	1.991	16.867	Furo-coumarins	Shikimates and Phenyl-propanoids

https://doi.org/10.1371/journal.pone.0340458.t002

Table 3. Effects of *n*-butanol fraction on the proliferation of cancer cells.

Cell line	Ethanol fraction (crude extract)	Dichloromethane fraction	*n*-Butanol fraction	Overall p-value
MCF7	79.3 (63.8–97.4)	60.5 (49.5–71.9)	60.2 (55.1–65.8)	< 0.05
MKN45	—	105.1 (85.9–127.6)	85.2 (73.5–98.7)	> 0.05
AGS	167.4 (138.6–204.3)	80.8 (56.8–110.5)	51.7 (45.1–58.3)	< 0.05

Data are presented as IC50 (95% confidence interval). Overall differences among treatments were assessed by one-way ANOVA.

https://doi.org/10.1371/journal.pone.0340458.t003

significant growth inhibition was recorded at concentrations of 100 μg/mL and above, where MKN45 cell viability dropped to 69.9 ± 17.2% ($p < 0.05$), while MCF-7 and AGS cell viabilities were markedly reduced to 48.1 ± 5.5% and 46.3 ± 5.2%, respectively ($p < 0.01$).

n-butanol fraction inhibits tumorsphere formation and growth of AGS gastric cancer cells

To assess the invasive potential of cancer cells, a 3D culture system was employed to induce the formation of tumorspheres, a characteristic closely associated with tumor maintenance and progression. The effects of the *n*-butanol fraction on tumorsphere formation are illustrated in Fig 4, with Fig 4C highlighting the impact of the extract on tumorsphere size.

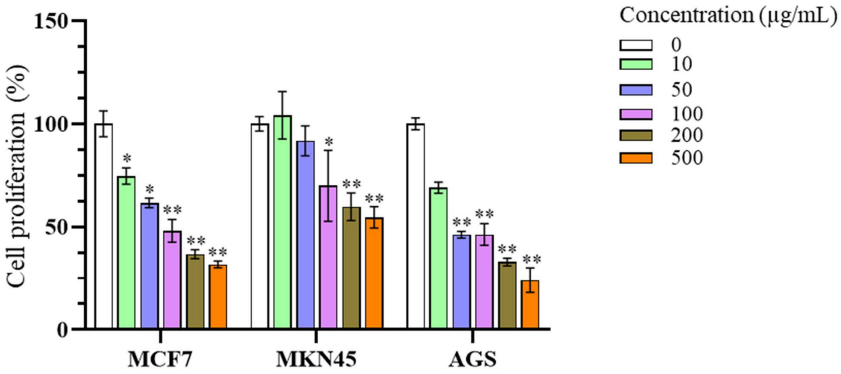

Fig 3. Effect of *n*-butanol fraction on cell proliferation of cancer cell lines. Cells were treated with the *n*-butanol fraction at various concentrations (0–500 µg/mL) for 48 h and subsequently analyzed using the MTT assay. Data are presented as mean ± SD. Statistical significance was assessed using the Mann–Whitney U test: $p < 0.05$, $p < 0.01$, and $p < 0.001$.

https://doi.org/10.1371/journal.pone.0340458.g003

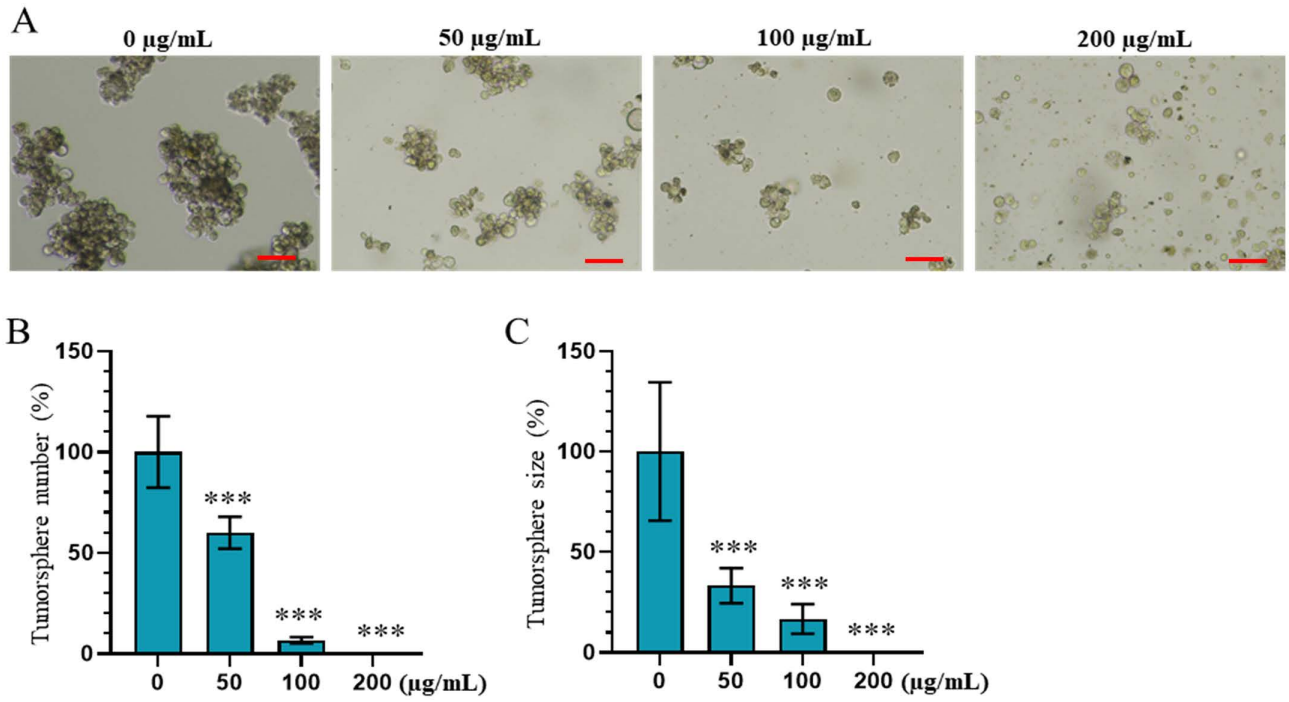

Fig 4. Effects of *n*-butanol fraction on the tumorsphere formation of AGS gastric cancer. (A) Effect of fraction on tumorsphere morphology, **(B)** on tumorsphere number, and **(C)** on tumorsphere size. Data are presented as the mean ± standard deviation, Mann-Whitney test, ***$p < 0.001$ compared to the control; Scale bar = 100 µm.

https://doi.org/10.1371/journal.pone.0340458.g004

The results demonstrate that both the number and size of tumorspheres decreased progressively with increasing concentrations of the extract (50–200 µg/mL). At a concentration of 50 µg/mL, a significant reduction in both tumorsphere number and size was observed compared to the control ($p < 0.01$). Upon increasing the concentration to 100 µg/mL, the number of tumorspheres dropped to approximately 5%, and their size was reduced to about 15% relative to the untreated group. Notably, at the highest tested concentration of 200 µg/mL, tumorsphere formation was almost completely inhibited. These

findings clearly indicate that under 3D culture conditions, the *n*-butanol fraction exerts a pronounced inhibitory effect on the tumorigenic capacity of cancer cells.

n-butanol fraction reduces migration ability of of AGS gastric cancer cells

The inhibitory effect of the *n*-butanol fraction on AGS gastric cancer cell migration is presented in Fig 5. The results revealed clear differences in cell migration based on the wound boundary observed in control wells compared to those treated with the *n*-butanol fraction. In the control group, AGS cells exhibited strong migratory activity, significantly

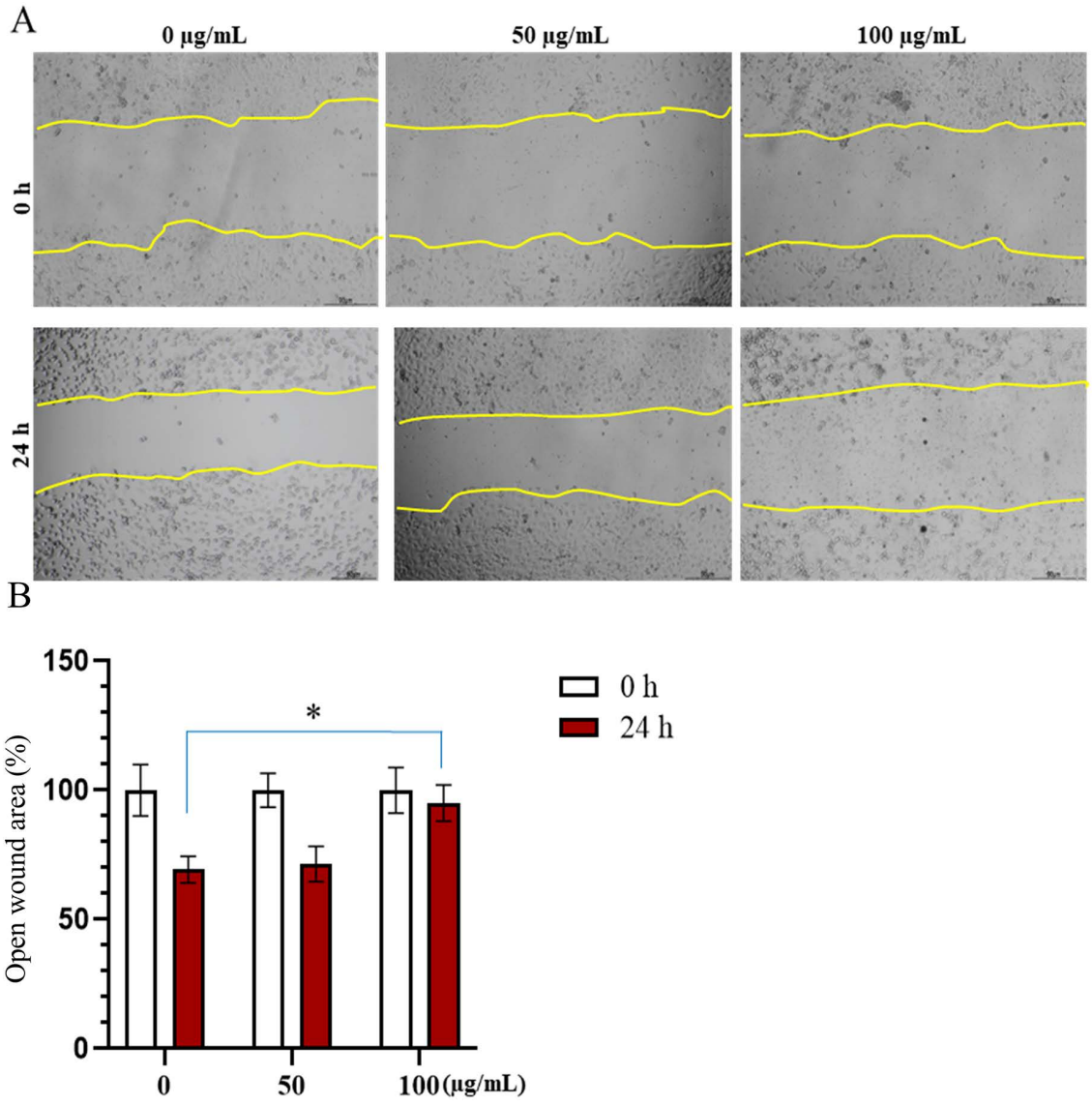

Fig 5. Effect of *n*-butanol fraction on the migration of AGS cells. (A) Representative images of wound healing assay showing the migratory ability of AGS cells treated with different concentrations (0, 50 and 100 µg/mL) of *n*-butanol fraction at 0 and 24 hours. The yellow lines delineate the wound edges. **(B)** Quantitative analysis of wound closure percentage at 0 and 24 hours. Data are presented as mean ± standard deviation. Mann-Whitney test, *$p < 0.05$, **$p < 0.01$ compared to the control group (0 µg/mL).

https://doi.org/10.1371/journal.pone.0340458.g005

narrowing the wound area after 24 hours, to approximately 70% of the initial width at 0 hours. At a concentration of 50 μg/mL, the extract did not result in a significant difference in migration compared to the untreated control. However, at a concentration of 100 μg/mL, a marked inhibition of cell migration was observed. Cells showed substantially reduced or complete absence of movement into the wound area, and most of the observed cells were either non-motile or dead. The measured wound widths in the 100 μg/mL treatment groups remained at approximately 95%, respectively, compared to the control group at 24 hours ($p < 0.05$). These findings suggest that the *n*-butanol fraction impairs the migratory capacity of AGS cells in a dose-dependent manner.

n-butatnol fraction induces cell senescence

The impact of the *n*-butanol fraction on cellular senescence in AGS cells is presented in Fig 6. Treatment with 50 μg/mL of the extract resulted in a marked increase in senescent cell number—approximately 25-fold compared to the control group ($p < 0.01$). At a higher concentration of 100 μg/mL, the extract induced the most pronounced senescence, as evidenced by a substantial accumulation of SA-β-gal-positive cells, showing an approximately 93-fold increase relative to the control ($p < 0.01$). Interestingly, at the highest concentration tested (200 μg/mL), the proportion of senescent cells significantly decreased compared to the 50 and 100 μg/mL treatments. Instead, a notable increase in cell death was observed, indicating a shift in the cellular response from senescence induction to cytotoxicity ($p < 0.05$).

n-butanol fraction induces cell cycle arrest at G0/G1 phase

The effects of the *n*-butanol fraction on the cell cycle were evaluated by flow cytometry analysis. Cell cycle profiling (Fig 7) revealed that the *n*-butanol fraction induced cell cycle arrest in AGS cells. Specifically, there was an accumulation of cells in the G0/G1 phase in the *n*-butanol-treated group (68.6 ± 2.7%) compared to the control group (57.7 ± 3.6%), respectively ($p < 0.05$). This was accompanied by a reduction in the S phase population ($p < 0.05$), indicating that the extract effectively induced G0/G1 phase arrest.

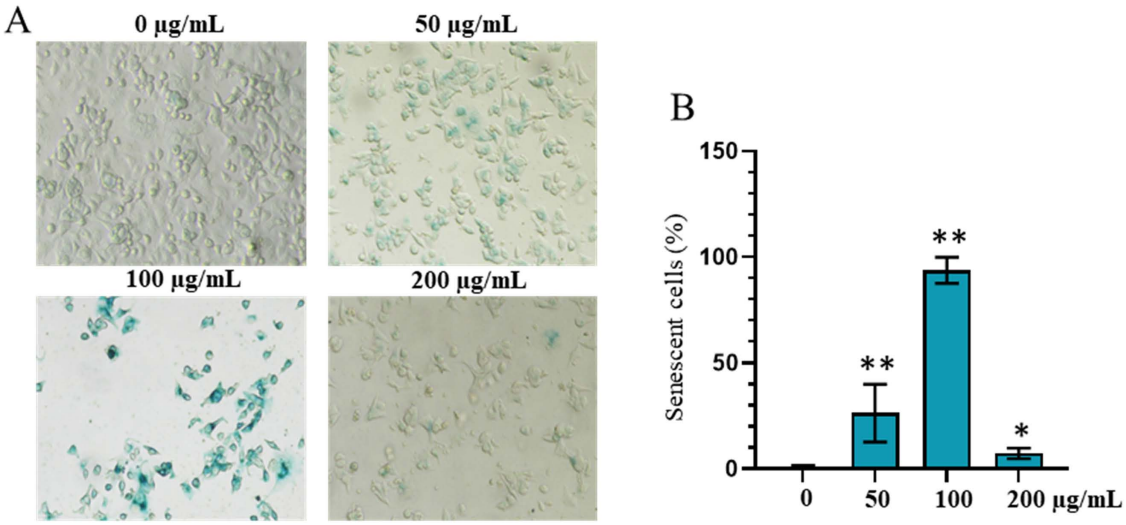

Fig 6. Effect of *n*-butanol frtion on cellular senescence in AGS gastric cancer cells. (A) Representative images of senescence-associated β-galactosidase (SA-β-gal) staining in AGS cells treated with different concentrations (0, 50, 100, and 200 μg/mL) of *n*-butanol fraction. Senescent cells are stained blue. **(B)** Quantitative analysis of the percentage of SA-β-gal-positive cells. Data are presented as mean ± standard deviation. Mann-Whitney test, *$p < 0.05$, **$p < 0.01$ compared to the control (0 μg/mL).

https://doi.org/10.1371/journal.pone.0340458.g006

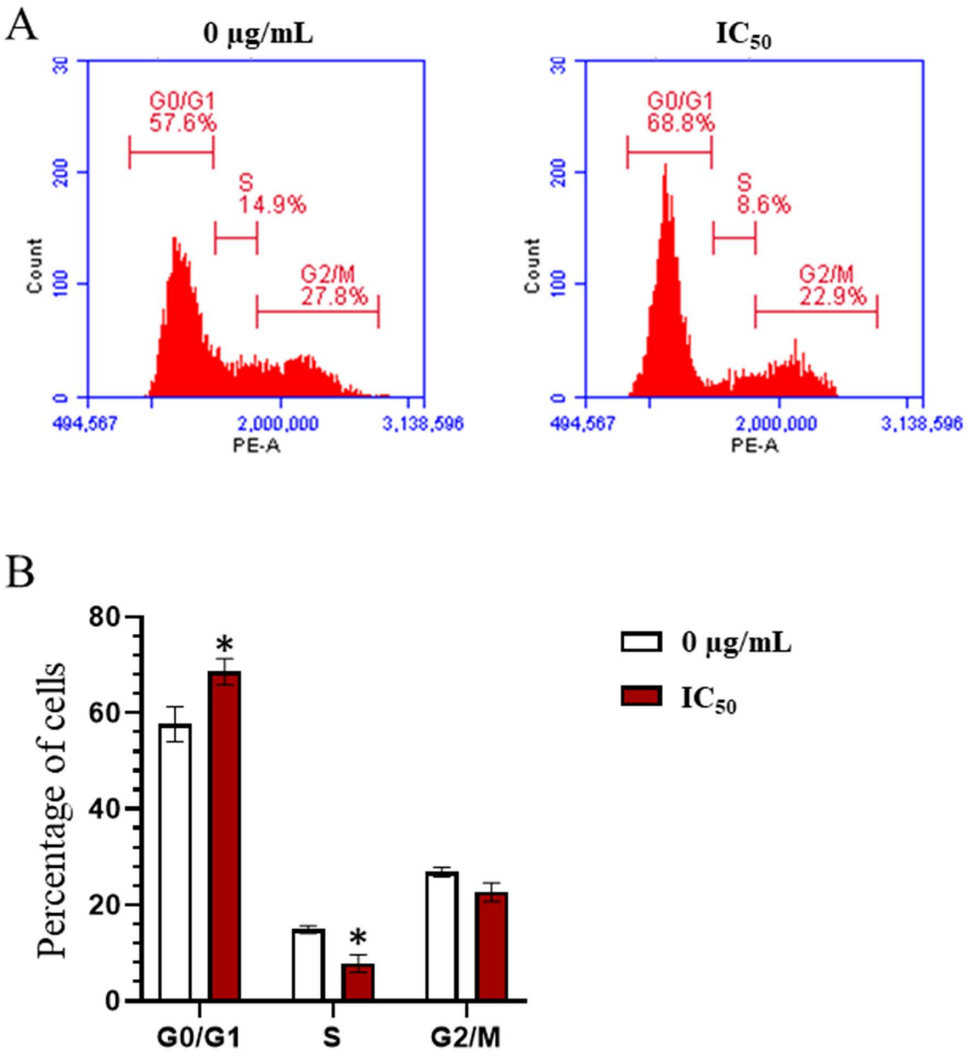

Fig 7. Effect of *n*-butanol fraction on AGS cell cycle. (A) Cell cycle analysis plots by flow cytometry showing the percentage of AGS cells in different phases after treatment with *n*-butanol fraction and the control group. **(B)** Quantitative analysis of the percentage of cells in G0/G1, S, and G2/M phases. Data are presented as the mean ± standard deviation, Mann-Whitney test, *p < 0.05.

https://doi.org/10.1371/journal.pone.0340458.g007

Real-time PCR analysis (Fig 8) showed that the *n*-butanol fraction at the IC_{50} concentration markedly altered the expression of cell cycle–related genes compared with the 0 μg/mL control. The *n*-butanol fraction significantly downregulated pro-proliferative cyclin genes, including CCND1, CCND2, and CCNE1, whereas CCNA2 and CCNB1 exhibited only minor or no apparent changes. In parallel, the expression of CDK family genes (CDK2, CDK3, CDK6, CDK8, and CDK9) was significantly reduced. Conversely, the *n*-butanol fraction significantly upregulated cell cycle inhibitory and anti-proliferative response genes such as P21, P53, P16, and P57, while P27 remained largely unchanged. Collectively, these data indicate that the *n*-butanol fraction suppresses cell proliferation primarily by inhibiting the Cyclin–CDK axis and activating cell cycle inhibitory signaling pathways.

Molecular docking. To evaluate the reliability of the docking protocol, re-docking experiments were conducted in which co-crystallized ligands were redocked into the active sites of their respective target proteins. In all cases, the

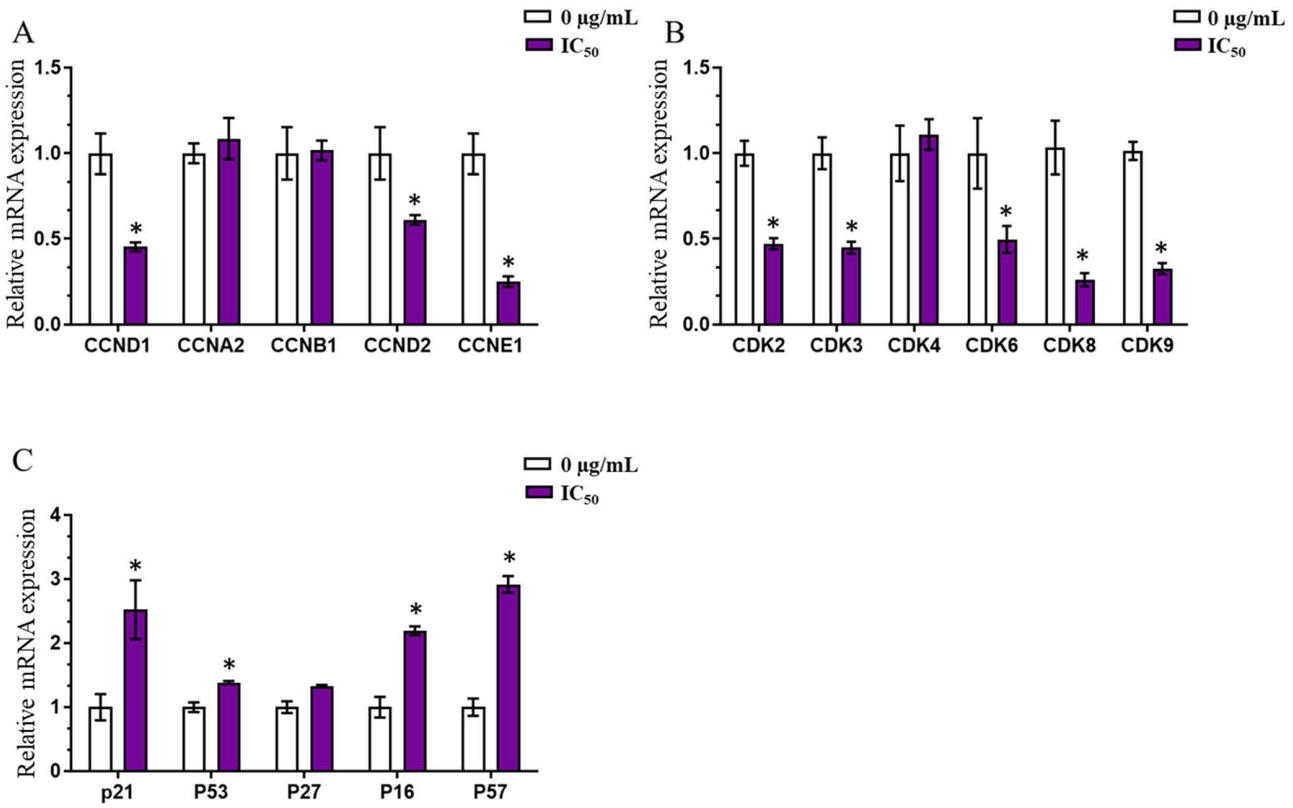

Fig 8. Effect of *n*-butanol fraction on cell cycle regulatory gene expression at mRNA level in AGS gastric cancer cells. Cells were treated with *n*-butanol fraction at concentration of IC_{50} (52.7 μg/mL) for 24 hours. RNA total was extracted for realtime PCR analysis. Changes in mRNA levels of genes were analysis by $2^{-\Delta\Delta Ct}$ method. **(A)** Bar graphs showing the expression of genes belonging to the cyclin group, **(B)** genes belonging to the cyclin-dependent kinase group, and **(C)** genes belonging to the cyclin inhibitor group. Data are presented as the mean ± standard deviation. All results are presented as mean ± SD (n = 3). Mann-Whitney test, *p < 0.05 compared to control (0 μg/mL).

https://doi.org/10.1371/journal.pone.0340458.g008

resulting RMSD values were below 2.0 Å, indicating high reproducibility and accuracy of the docking methodology employed in this study. A total of 118 compounds identified from *Ardisia villosa n*-butanol fraction were subjected to virtual screening against six cell cycle-regulating cyclin-dependent kinases (CDK2, CDK3, CDK4, CDK6, CDK8, and CDK9) using the Glide XP, followed by rescoring with Prime MM-GBSA to refine binding energy estimates. A comprehensive overview of the MM-GBSA results is presented in Fig 9. Each data point corresponds to a ligand–protein complex, with the x-axis indicating compound index (from 1 to 118), the y-axis representing MM-GBSA values (kcal/mol), and color-coding distinguishing among the six CDK targets. This visualization facilitates the comparative analysis of binding affinity distributions across targets.

The majority of ligands displayed binding free energies in the range of −25 to −50 kcal/mol. Specifically, the number of compounds within this range were: CDK2 (59 compounds), CDK3 (26), CDK4 (67), CDK6 (72), CDK8 (63), and CDK9 (65). Notably, the proportion of compounds exhibiting ΔG_{bind} values below −50 kcal/mol ranged from 2.54% to 17.8%, depending on the target. CDK8 had the highest number of strong binders (21 compounds), while CDK2 had the fewest (only 3 compounds).

From this dataset, the top-scoring ligand for each CDK was identified based on the lowest ΔGbind score. Compound 26 emerged as the strongest binder for both CDK2 (−65.812 kcal/mol) and CDK4 (−58.926 kcal/mol). The

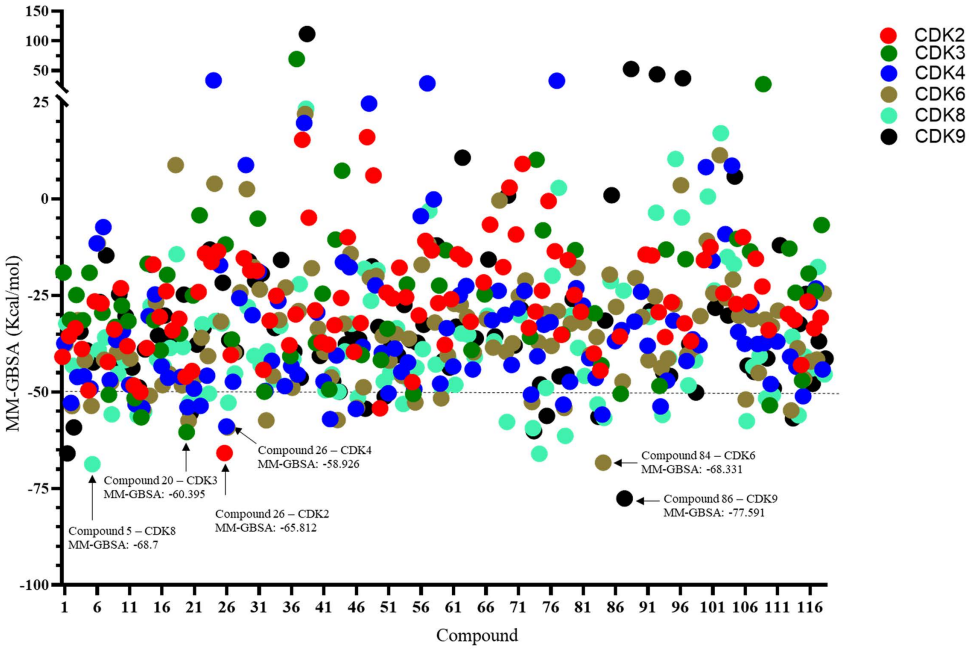

Fig 9. Molecular docking analysis results of compounds from the *n*-butanol fraction with cyclin-dependent proteins.

https://doi.org/10.1371/journal.pone.0340458.g009

highest-affinity ligands for the remaining targets were: compound 20 for CDK3 (−60.395 kcal/mol), compound 84 for CDK6 (−68.331 kcal/mol), compound 5 for CDK8 (−68.7 kcal/mol), and compound 87 for CDK9 (−77.591 kcal/mol). A detailed summary of binding affinities and molecular interaction profiles for these ligand–target complexes is provided in Table 4. Fig 10 illustrates representative 2D and 3D spatial interactions of each ligand within the active site of its corresponding protein.

Table 4. Docking Scores, and MM-GBSA energies of compounds from *n*-butanol fraction with target CDK proteins.

Protein	Ligand(compound)	Docking score (kcal/mol)	MM-GBSA (kcal/mol)	Hydrophilic	Hydrophobic	Electrostatic
CDK2	**Lappaol H**	−10.681	−65.812	LYS89, GLU8, GLU12, ILE10, GLN131,LEU8, LYS33, HIS84, GLU162, LYS9	ALA31, ILE10, LYS9, VAL64, LEU134, VAL18	GLU8
CDK3	**3-O-Methylellagic acid**	−7.952	−60.395	LYS22, ASP97, GLU144,ASN145, VAL14, GLU11	ALA10, VAL72, LYS22	
CDK4	**Lappaol H**	−10.311	−58.926	LYS147, GLN149, ASP104, VAL101, THR182, HIS100, LYS147, GLN149, TYR24	ILE19, LEU152, ALA41	
CDK6	**Cistanoside C**	−10.306	−68.331	LYS147, GLN149, ASP104, VAL101, THR182, HIS100, TYR24	ILE19, LEU152, ALA41	
CDK8	**Nordracorubin**	−6.515	−68.7	LYS153	TYR32, VAL27, VAL35, ALA50, ALA100, LEU158, LYS52, ALA172	
CDK9	**Hordatine B**	−9.573	−77.591	ASP167, ASP109, PHE168, GLU66, ASP149, ASN154, PHE105, ASP154, ASP104, GLU107	PHE103, ALA46, VAL79, CYS106, LEU156, ILE25, ALA46, ALA166	ASP167, ASP109, ASP149

https://doi.org/10.1371/journal.pone.0340458.t004

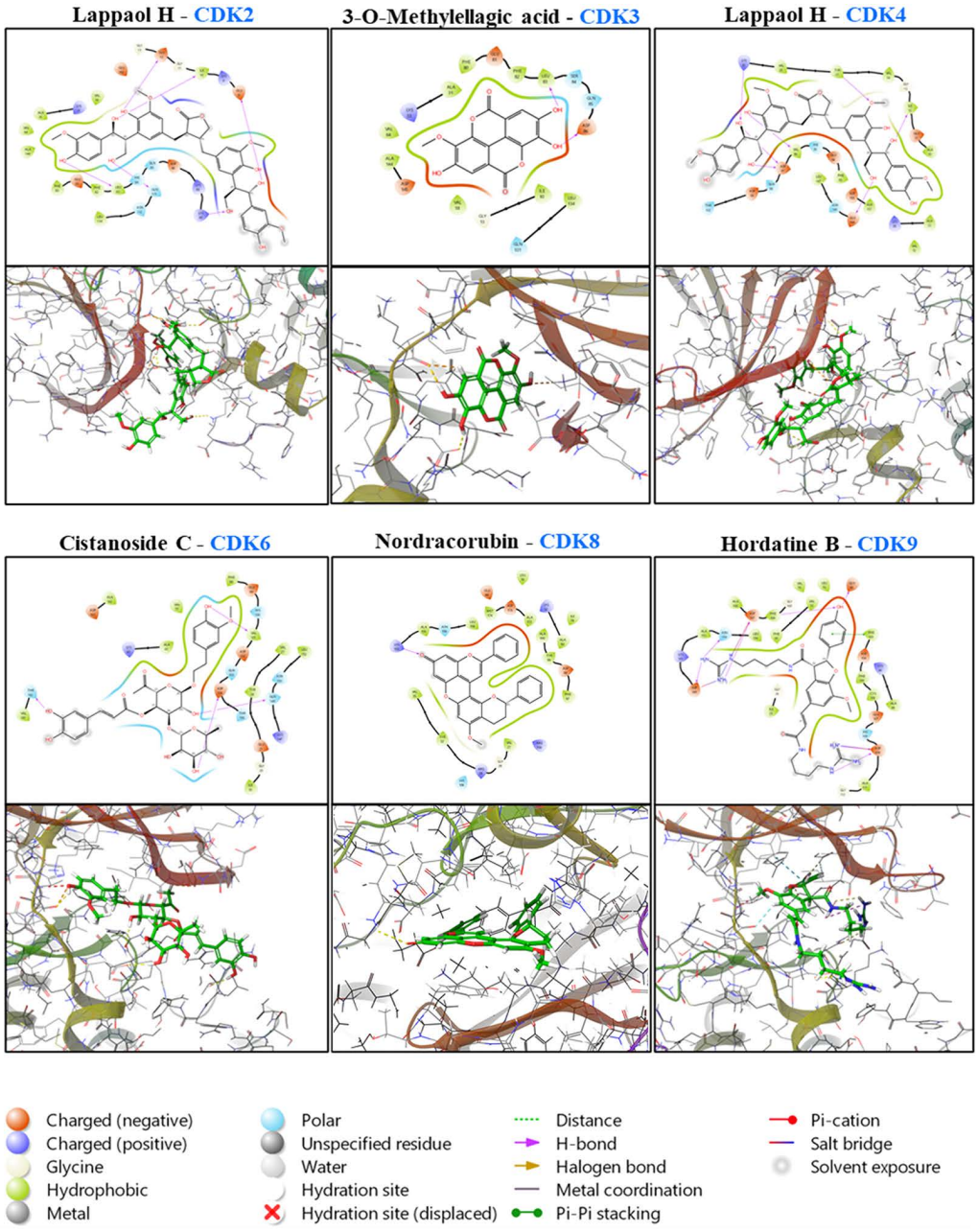

Fig 10. 2D and 3D interaction diagrams of the compounds with the target proteins exhibiting the highest binding energies.

https://doi.org/10.1371/journal.pone.0340458.g010

Discussion

Accurate identification of the chemical constituents present in plant extracts is critically important for predicting and evaluating their potential biological activities. In this study, ultra-performance liquid chromatography coupled with quadrupole time-of-flight mass spectrometry (UPLC-QToF-MS) was employed for the chemical profiling of the *n*-butanol fraction obtained from *Ardisia villosa* leaves. This analytical technique offers high sensitivity and precision; a signal intensity

threshold of >5000 counts and a mass error tolerance of 5 ppm were applied to ensure the reliable detection and identification of constituents in the extract.

Mass spectrometric analysis revealed a diverse array of metabolites, with a total of 118 compounds identified. These compounds were classified into various chemical categories, including triterpenoids (37 compounds), alkaloids (22 compounds), flavonoids (10 compounds), lignans (10 compounds), steroids (13 compounds), coumarins (5 compounds), phenolic and aromatic compounds (12 compounds), along with other functional constituents. Notably, there has been limited prior research on the phytochemical composition of *Ardisia villosa*, and thus, the majority of the 118 identified compounds are reported here for the first time, made possible by the high sensitivity of the UPLC-QToF-MS platform.

Significantly, numerous compounds identified and enumerated in Table 1 have been previously documented to demonstrate anticancer activity across various cancer cell lines. For example, within the flavonoid and phenolic groups, notable compounds include ononin (compound 3) [22], epigallocatechin-(4β→8)-gallocatechin (compound 17) [23], icariin (compound 83) [24], and sanggenon C (compound 105) [25]. Among the terpenoids and steroids, compounds such as bruceene (6), ganoderenic acid A (25) [26], cucurbitacin B (67) [27], and simalikalactone D (81) [28] were identified. In the alkaloid category, brucine (75) [29], Pingpeimine A (91) [30], và Neferine (93) [31] were detected.

The anticancer activity of the *n*-butanol fraction was evaluated against three different cancer cell lines MCF-7, MKN45, and AGS, and the results demonstrated that the extract exhibited the highest sensitivity toward AGS cells, with an IC_{50} value of 51.7 ± 2.8 μg/mL. Previous cytotoxicity studies on other *Ardisia* species reported that an ethanol extract from *Ardisia gigantifolia* exerted inhibitory effects on gastric cancer cell lines MKN45 and MKN74, with IC_{50} values of 55.7 and 123.6 μg/mL, respectively [12]. In addition, earlier investigations revealed that the *n*-butanol fraction of *Pterocephalus hookeri* displayed cytotoxic effects on the Hep3B liver cancer cell line (IC_{50} = 90.8 μg/mL) and Caco-2 colorectal cancer cells (IC_{50} = 175.2 μg/mL) [32].

These findings suggest that the antiproliferative potency of plant extracts can vary significantly depending on both the plant species and the extraction solvent used. Differences in solvent polarity and chemical affinity may lead to the enrichment of distinct sets of bioactive compounds, which ultimately influence the biological activity of the extracts.

In recent years, the 3D tumorsphere model has been considered superior to conventional 2D culture systems for toxicity testing due to its high physiological relevance to in vivo tumors. This model allows for more accurate evaluation of drug efficacy and enhances the screening potential for novel therapeutic agents [33,34]. In this study, the *n*-butanol fraction markedly inhibited tumorsphere formation in AGS gastric cancer cells, underscoring its broad-spectrum anticancer potential. The observed reduction in both the number and size of tumorspheres suggests that bioactive compounds in this fraction effectively target even highly proliferative subpopulations within the tumorspheres.

Cells capable of forming tumorspheres have previously been shown to exhibit cancer stem cell-like properties [34], implying that the butanol fraction may modulate critical signaling pathways essential for cancer stem cell survival and maintenance. Further studies are warranted to elucidate these underlying mechanisms. Cell migration is a key indicator of tumor cell viability, invasiveness, and metastatic potential [34]. In the present study, migration analysis revealed that the n-butanol fraction significantly suppressed the ability of AGS cancer cells to migrate into the wound area created on the culture plate surface. These findings are consistent with earlier results showing that the *n*-butanol fraction reduced AGS cell proliferation and are also in agreement with previous studies reporting anticancer activity of *n*-butanol fraction from *Ricinus communis* in MCF-7 breast cancer cells [35], and the Wenxia Formula Extract in H460 and A549 lung cancer cell lines [36].

Cellular senescence is increasingly recognized as a promising strategy in the development of next-generation cancer therapies. By shifting cancer cells from an uncontrolled proliferative state to an irreversible growth arrest, senescence can effectively impede tumor progression [35]. A key objective of this study was to investigate whether the *n*-butanol fraction could induce senescence in AGS gastric cancer cells.

Our findings revealed that treatment with the *n*-butanol fraction at concentrations of 50 and 100 μg/mL induced a pronounced senescent phenotype in AGS cells. In contrast, at higher concentrations (e.g., 200 μg/mL), senescent cells were no longer observed, and instead, a significant increase in cell death was detected, suggesting a shift from a senescence-inducing effect to a cytotoxic response. This concentration-dependent relationship between senescence and cell death aligns with established mechanisms in which sub-lethal drug exposure promotes senescence, whereas higher concentrations trigger apoptosis or necrosis [36].

The data indicate that the *n*-butanol fraction can induce either cellular senescence or apoptosis, contingent upon the administered dose. Both mechanisms contribute to the inhibition of cancer cell proliferation and may present a dual-mode therapeutic advantage.

As previously mentioned, cellular senescence is characterized by irreversible cell cycle arrest, often associated with the accumulation of cells in the quiescent G0 phase. This hypothesis was investigated through cell cycle analysis (Fig 7). A notable increase in the proportion of cells in the G0/G1 phase compared to the control group indicates that the *n*-butanol fraction delays cell cycle progression—a critical mechanism contributing to senescence induction.

Further validation using real-time PCR analysis revealed a marked downregulation of several key genes involved in cell cycle progression, particularly those belonging to the cyclin family (CCND1, CCND2, CCNE1) and cyclin-dependent kinases (CDK2, CDK3, CDK6, CDK8, and CDK9), all of which play essential roles in regulating cell proliferation and oncogenesis As previously mentioned, cellular senescence is characterized by irreversible cell cycle arrest, often associated with the accumulation of cells in the quiescent G0 phase. This hypothesis was investigated through cell cycle analysis (Fig 7). A notable increase in the proportion of cells in the G0/G1 phase compared to the control group indicates that the *n*-butanol fraction delays cell cycle progression—a critical mechanism contributing to senescence induction.

Further validation using real-time PCR analysis revealed a marked downregulation of several key genes involved in cell cycle progression, particularly those belonging to the cyclin family (CCND1, CCND2, CCNE1) and cyclin-dependent kinases (CDK2, CDK3, CDK6, CDK8, and CDK9), all of which play essential roles in regulating cell proliferation and oncogenesis [37].

Remarkably, genes encoding major negative regulators of the cell cycle and established markers of cellular senescence, including p21, p53, p16, and p57, were significantly upregulated following treatment [38,39]. These findings indicate that the *n*-butanol fraction modulates the expression of both pro-proliferative and anti-proliferative genes, thereby promoting cell cycle arrest and senescence in AGS gastric cancer cells.

In addition to the observed transcriptional downregulation of cyclin and CDK genes, we hypothesized that certain compounds present in the *n*-butanol fraction of *Ardisia villosa* may directly inhibit the activity of CDK proteins through high-affinity binding to their active sites. Based on MM-GBSA binding free energy values obtained from in silico molecular docking analyses, several compounds within the extract demonstrated strong potential for CDK inhibition, with binding energies below –50 kcal/mol. Notably, compounds such as Lappaol H, 3-O-Methylellagic acid, Cistanoside C, Nordracorubin, and Hordatine B exhibited the strongest binding affinities toward CDK family proteins, including CDK2, CDK3, CDK4, CDK6, CDK8, and CDK9.

Previous experimental studies have reported that a compound from the Lappaol family, Lappaol F, induces cell cycle arrest at the S phase in colorectal cancer cells [40], and at the G1 and G2 phases in other cancer cell lines [37]. While experimental evidence supporting the cell cycle inhibitory activity of the other identified compounds is currently lacking, their high binding affinity to CDK proteins strongly suggests that they may serve as promising CDK inhibitors. These findings highlight the potential of these natural compounds as candidates for further investigation in cell-based assays to validate their anticancer mechanisms. However, the limitation of this study is that the biological activity assessments were mainly conducted through in vitro experiments, without in vivo validation or isolation of individual bioactive compounds. Moreover, the molecular docking predictions are only theoretical and require further verification through the isolation of pure compounds followed by experimental evaluation of their biological activities in both *in vitro* and *in vivo* models.

Conclusion

The c of *Ardisia villosa* demonstrates notable anticancer activity through inhibition of cell proliferation, tumorsphere formation, and migration, as well as induction of cellular senescence. Phytochemical analysis revealed a diverse profile of bioactive compounds. These findings support its potential as a natural anticancer agent and warrant further preclinical investigation to elucidate its therapeutic efficacy and underlying mechanisms.

Supporting information

S1 Table. List of primer for Real-time PCR.
(DOCX)

S2 Table. Effect of the ethanol extract on cancer cell proliferation.
(DOCX)

S3 Table. Effect of the n-butanol fraction on cancer cell proliferation.
(DOCX)

S4 Table. Effect of the dichloromethane fraction on cancer cell proliferation.
(DOCX)

Author contributions

Conceptualization: Van Khang Pham, Phu Hung Nguyen.

Data curation: Nguyet Mai Hua, Thi Thanh Huong Le, Son hiep Pham, Viet Hoang, Thu Huong Trinh, Dinh Quang Hung Can.

Formal analysis: Nguyet Mai Hua, Van Khang Pham, Thi Thanh Huong Le, Son hiep Pham, Viet Hoang, Thu Huong Trinh, Dinh Quang Hung Can, Phu Hung Nguyen.

Funding acquisition: Thi Thanh Huong Le, Phu Hung Nguyen.

Investigation: Nguyet Mai Hua, Thi Thanh Huong Le, Phu Hung Nguyen.

Methodology: Van Hung Hoang, Phu Hung Nguyen.

Supervision: Van Khang Pham, Phu Hung Nguyen.

Validation: Phu Hung Nguyen.

Visualization: Van Hung Hoang.

Writing – original draft: Nguyet Mai Hua, Van Khang Pham, Thi Thanh Huong Le, Viet Hoang, Van Hung Hoang, Phu Hung Nguyen.

Writing – review & editing: Van Hung Hoang, Phu Hung Nguyen.

References

1. Siegel RL, Giaquinto AN, Jemal A. Cancer statistics, 2024. CA Cancer J Clin. 2024;74(1):12–49. https://doi.org/10.3322/caac.21820 PMID: 38230766
2. Bray F, Laversanne M, Sung H, Ferlay J, Siegel RL, Soerjomataram I, et al. Global cancer statistics 2022: GLOBOCAN estimates of incidence and mortality worldwide for 36 cancers in 185 countries. CA Cancer J Clin. 2024;74(3):229–63. https://doi.org/10.3322/caac.21834 PMID: 38572751
3. Arnold M, Park JY, Camargo MC, Lunet N, Forman D, Soerjomataram I. Is gastric cancer becoming a rare disease? A global assessment of predicted incidence trends to 2035. Gut. 2020;69(5):823–9. https://doi.org/10.1136/gutjnl-2019-320234 PMID: 32001553

4. Li Y-N, Xie B, Zhang Y, He M-H, Xing Y, Mu D-M, et al. Advances and key focus areas in gastric cancer immunotherapy: A comprehensive scientometric and clinical trial review (1999-2023). World J Gastroenterol. 2023;29(40):5593–617. https://doi.org/10.3748/wjg.v29.i40.5593 PMID: 37970478
5. Tohme S, Simmons RL, Tsung A. Surgery for Cancer: A Trigger for Metastases. Cancer Res. 2017;77(7):1548–52. https://doi.org/10.1158/0008-5472.CAN-16-1536 PMID: 28330928
6. López MJ, Carbajal J, Alfaro AL, Saravia LG, Zanabria D, Araujo JM, et al. Characteristics of gastric cancer around the world. Crit Rev Oncol Hematol. 2023;181:103841. https://doi.org/10.1016/j.critrevonc.2022.103841 PMID: 36240980
7. Joshi DC, Sharma A, Prasad S, Singh K, Kumar M, Sherawat K, et al. Novel therapeutic agents in clinical trials: emerging approaches in cancer therapy. Discov Oncol. 2024;15(1):342. https://doi.org/10.1007/s12672-024-01195-7 PMID: 39127974
8. Schirrmacher V. From chemotherapy to biological therapy: A review of novel concepts to reduce the side effects of systemic cancer treatment (Review). Int J Oncol. 2019;54(2):407–19. https://doi.org/10.3892/ijo.2018.4661 PMID: 30570109
9. Liu B, Liu R, Liu Q, Ashby CR Jr, Zhang H, Chen Z-S. The ethnomedicinal and functional uses, phytochemical and pharmacology of compounds from Ardisia species: An updated review. Med Res Rev. 2022;42(5):1888–929. https://doi.org/10.1002/med.21894 PMID: 35670013
10. Tian-Liang, Xie Q, Shama R, Yu J, Xi-Gu-Ri-Gan, Bao Q, et al. Ethnobotanical study of Zhuang medicinal herbs of Ardisia: variety systematization, traditional uses, phytochemistry, pharmacology, clinical application, and toxicity. J Pharm Pharmacol. 2024;76(4):327–53. https://doi.org/10.1093/jpp/rgad119 PMID: 38402634
11. Yen C-H, Lin C-J, Chen P-Y, Chen Y-J, Wei L-R, Chen P-H, et al. Taming Pancreatic Cancer: Ardisia virens Kurz-Derived 4-Hydroxy-2-Methoxy-6-Tridecylphenyl Acetate as a Potent Tubulin Polymerization Inhibitor for Targeted Pancreatic Ductal Adenocarcinoma Therapy. Int J Med Sci. 2025;22(3):651–61. https://doi.org/10.7150/ijms.104112 PMID: 39898251
12. Le TT, Nguyen PH, Nguyen VP, Nguyen TN. Ardisia gigantifolia ethanolic extract inhibits cell proliferation and targets cancer stem cells in gastric cancer. Asian Pacific Journal of Tropical Biomedicine. 2023;13(6):258–67. https://doi.org/10.4103/2221-1691.378600
13. Liu B, Liu R, Liu Q, Ashby CR Jr, Zhang H, Chen Z-S. The ethnomedicinal and functional uses, phytochemical and pharmacology of compounds from Ardisia species: An updated review. Med Res Rev. 2022;42(5):1888–929. https://doi.org/10.1002/med.21894 PMID: 35670013
14. Hương LTT, Khang PV, Hiền HTT, Hùng NP. Hoạt Tính Ức Chế Sự Tăng Sinh Tế Bào Của Dịch Chiết Từ Lá Cây Cơm Nguội Lông (ardisia Villosa) Trên Tế Bào Ung Thư Dạ Dày Mkn45. TNUJST. 2021;226(10):365–71. https://doi.org/10.34238/tnu-jst.4612
15. Nguyen PH, Le TTH, Can DQH, Le TNT, Hoang V, Ngo HP, et al. Anticancer potential of Ampelopsis cantoniensis extract: Inducing apoptosis, cell cycle arrest, and targeting cancer stem cells in HepG2 liver cancer cells. Biocatalysis and Agricultural Biotechnology. 2025;64:103521. https://doi.org/10.1016/j.bcab.2025.103521
16. Vu TX, Tran TB, Vu H-H, Le YTH, Nguyen PH, Do TT, et al. Ethanolic extract from fruiting bodies of Cordyceps militaris HL8 exhibits cytotoxic activities against cancer cells, skin pathogenic yeasts, and postharvest pathogen Penicillium digitatum. Arch Microbiol. 2024;206(3):97. https://doi.org/10.1007/s00203-024-03833-8 PMID: 38349544
17. Nong TAT, Le TTH, Vu VT, Nguyen MQ, Can DQH, Dong THY, et al. Inhibitory Activity of Compounds Isolated from Ligustrum robustum (Roxb.) Against HepG2 Liver Cancer Cells: Isocubein and 4-(2-Acetoxyethyl)phenol as Potential Candidates. Chem Biodivers. 2024;21(10):e202401065. https://doi.org/10.1002/cbdv.202401065 PMID: 39004876
18. Huong Le TT, Nguyen MQ, Nguyen VP, Hoang VH, Nguyen PH. Methanol Extract of Ficus pumila L. Inhibits Proliferation, Induces Apoptosis and Arrests the Cell Cycle in HepG2 Live Cancer Cells. Asian J of Plant Sciences. 2023;22(3):423–33. https://doi.org/10.3923/ajps.2023.423.433
19. Hoang VH, Le TTH, Nguyen PH, Nguyen DH, Luc QT, Nguyen TKO, et al. Anticancer activity of Elsholtzia winitiana var. dongvanensis Phuong on gastric cancer cells: phytochemical profiling, cell proliferation inhibition, senescence induction, and cell cycle arrest. Beni-Suef Univ J Basic Appl Sci. 2025;14(1). https://doi.org/10.1186/s43088-025-00634-w
20. Livak KJ, Schmittgen TD. Analysis of relative gene expression data using real-time quantitative PCR and the 2(-Delta Delta C(T)) Method. Methods. 2001;25(4):402–8. https://doi.org/10.1006/meth.2001.1262 PMID: 11846609
21. Genheden S, Ryde U. The MM/PBSA and MM/GBSA methods to estimate ligand-binding affinities. Expert Opin Drug Discov. 2015;10(5):449–61. https://doi.org/10.1517/17460441.2015.1032936 PMID: 25835573
22. Sharma U, Sharma B, Mishra A, Sahu A, Mathkor DM, Haque S, et al. Ononin: A comprehensive review of anticancer potential of natural isoflavone glycoside. J Biochem Mol Toxicol. 2024;38(6):e23735. https://doi.org/10.1002/jbt.23735 PMID: 38773908
23. Markowska A, Antoszczak M, Markowska J, Huczyński A. Role of Epigallocatechin Gallate in Selected Malignant Neoplasms in Women. Nutrients. 2025;17(2):212. https://doi.org/10.3390/nu17020212 PMID: 39861342
24. Liu F-Y, Ding D-N, Wang Y-R, Liu S-X, Peng C, Shen F, et al. Icariin as a potential anticancer agent: a review of its biological effects on various cancers. Front Pharmacol. 2023;14:1216363. https://doi.org/10.3389/fphar.2023.1216363 PMID: 37456751
25. Huang H, Liu N, Zhao K, Zhu C, Lu X, Li S, et al. Sanggenon C decreases tumor cell viability associated with proteasome inhibition. Front Biosci (Elite Ed). 2011;3(4):1315–25. https://doi.org/10.2741/E335 PMID: 21622138
26. Chen S, Chen K, Lin Y, Wang S, Yu H, Chang C, et al. Ganoderic acid T, a Ganoderma triterpenoid, modulates the tumor microenvironment and enhances the chemotherapy and immunotherapy efficacy through downregulating galectin-1 levels. Toxicol Appl Pharmacol. 2024;491:117069. https://doi.org/10.1016/j.taap.2024.117069 PMID: 39142358

27. Dai S, Wang C, Zhao X, Ma C, Fu K, Liu Y, et al. Cucurbitacin B: A review of its pharmacology, toxicity, and pharmacokinetics. Pharmacol Res. 2023;187:106587. https://doi.org/10.1016/j.phrs.2022.106587 PMID: 36460279
28. Mendez B, Reyes J, Conde I, Ramos Z, Lozada E, Cruz AM, et al. Simalikalactone D, a Potential Anticancer Compound from Simarouba tulae, an Endemic Plant of Puerto Rico. Plants (Basel). 2020;9(1):93. https://doi.org/10.3390/plants9010093 PMID: 31940804
29. Fan G, Liang X, He Y, Ren H, Zhao J, Liang T, et al. Brucine Sensitizes HepG2 Human Liver Cancer Cells to 5-fluorouracil via Fas/FasL Apoptotic Pathway. International J of Pharmacology. 2017;13(3):323–31. https://doi.org/10.3923/ijp.2017.323.331
30. Lei J, Yang J, Cheng S, Lu F, Wu Z, Wang Z, et al. Peimine induces apoptosis of glioblastoma cells through regulation of the PI3K/AKT signaling pathway. Exp Ther Med. 2024;28(6):447. https://doi.org/10.3892/etm.2024.12737 PMID: 39430343
31. Zhong P-C, Liu Z-W, Xing Q-C, Chen J, Yang R-P. Neferine inhibits the development of lung cancer cells by downregulating TGF-β to regulate MST1/ROS-induced pyroptosis. Kaohsiung J Med Sci. 2023;39(11):1106–18. https://doi.org/10.1002/kjm2.12752 PMID: 37698291
32. Guo C, Wu Y, Zhu Y, Wang Y, Tian L, Lu Y, et al. In Vitro and In Vivo Antitumor Effects of n-Butanol Extracts of Pterocephalus hookeri on Hep3B Cancer Cell. Evid Based Complement Alternat Med. 2015;2015:159132. https://doi.org/10.1155/2015/159132 PMID: 26089933
33. Rauner G, Gupta PB, Kuperwasser C. From 2D to 3D and beyond: the evolution and impact of in vitro tumor models in cancer research. Nat Methods. 2025;22(9):1776–87. https://doi.org/10.1038/s41592-025-02769-1 PMID: 40715728
34. Fotinós J, Marks MP, Barberis L, Vellón L. Assessing the distribution of cancer stem cells in tumorspheres. Sci Rep. 2024;14(1):11013. https://doi.org/10.1038/s41598-024-61558-6 PMID: 38745039
35. Colucci M, Sarill M, Maddalena M, Valdata A, Troiani M, Massarotti M, et al. Senescence in cancer. Cancer Cell. 2025;43(7):1204–26. https://doi.org/10.1016/j.ccell.2025.05.015 PMID: 40513577
36. Sun J-Y, Zhao J, Qiu Y, Fan T-J. Different concentrations of betaxolol switch cell fate between necroptosis, apoptosis, and senescence in human corneal stromal cells. Chem Biol Interact. 2024;391:110898. https://doi.org/10.1016/j.cbi.2024.110898 PMID: 38325520
37. Sun Q, Liu K, Shen X, Jin W, Jiang L, Sheikh MS, et al. Lappaol F, a novel anticancer agent isolated from plant arctium Lappa L. Mol Cancer Ther. 2014;13(1):49–59. https://doi.org/10.1158/1535-7163.MCT-13-0552 PMID: 24222662
38. Bringold F, Serrano M. Tumor suppressors and oncogenes in cellular senescence. Exp Gerontol. 2000;35(3):317–29. https://doi.org/10.1016/s0531-5565(00)00083-8 PMID: 10832053
39. Liu B, Peng Z, Zhang H, Zhang N, Liu Z, Xia Z, et al. Regulation of cellular senescence in tumor progression and therapeutic targeting: mechanisms and pathways. Mol Cancer. 2025;24(1):106. https://doi.org/10.1186/s12943-025-02284-z PMID: 40170077
40. Yang R-Y, Tan J-Y, Liu Z, Shen X-L, Hu Y-J. Lappaol F regulates the cell cycle by activating CDKN1C/p57 in human colorectal cancer cells. Pharm Biol. 2023;61(1):337–44. https://doi.org/10.1080/13880209.2023.2172048 PMID: 36708218